Trial functions for reduced-order models of piezoelectrically actuated MEMS tunable lenses

Mahmoud A. Farghaly, Ulrik Hanke, Muhammad N. Akram,
Einar Halvorsen
Department of Microsystems
University of Southeast Norway
Raveien 215
3184 Borre, Norway

Trial functions for reduced-order models of piezoelectrically actuated MEMS tunable lenses

Mahmoud A. Farghaly[a]**, Ulrik Hanke**[a]**, Muhammad N. Akram**[a]**, Einar Halvorsen**[a,*]

[a]Department of Microsystems, University of Southeast Norway, Raveien 215, 3184, Borre, Norway

Abstract. Piezoelectrically actuated MEMS lens structures can be composed of a clamped square elastic diaphragm partially covered with a thin piezoelectric film leaving a circular transparent region to form a lens pupil. To model these lenses' linear static optoelectromechanical performance, the displacement can be approximated by a linear combination of basis functions, *e.g.*, weighted Gegenbauer polynomials that satisfy clamped boundary conditions along the diaphragm edges. However, such a model needs as much as 120 degrees of freedom (DOFs) to provide a good approximation of the lens optical performance. To improve on this, we here consider approximating the deflection by an expansion using piecewise smooth functions that have different forms in the pupil and the actuator regions. We use exact solutions for the elastic plate differential equation over circular and annular subdomains, and weighted Gegenbauer polynomials in the remaining region. The latter enforces the boundary conditions. We have found that the larger the diaphragm area with exact plate solutions is, the lower is the number of DOFs needed to predict mechanical and optical quantities accurately. For example, a model with 10 DOFs achieves accuracies of 5.1% and 2.1% respectively for RMS wavefront error and reciprocal F-number for all pupil openings of interest.

*Einar Halvorsen, einar.Halvorsen@usn.no

1 Introduction

Tunable focus in cameras enables capture of sharp images over a wide range of camera-object distances and is considered an essential feature in modern cameras. Voice coil motors[1] and ultrasonic motors[2] are widely commercialized macro-scale technologies for tuning focus in devices such as mobile cameras. However, microelectromechanical systems (MEMS) lenses[3–8] promise low-power, small footprint mechanisms utilized for the same purpose.

In this paper, we consider piezoelectrically actuated MEMS tunable lenses.[3] Such a lens has a diaphragm consisting of a square glass plate covered by a thin piezoelectric film with a circular opening in the film leaving the central part transparent. When the piezoelectric film is biased, the diaphragm bends and a plano-convex lens is formed by a high-refractive index polymer sandwiched between the diaphragm and a second transparent plate.

Mathematical models are necessary for design and optimization of such MEMS devices and involve solving coupled multiphysics problems. A possible solution to this challenge is to use numerical calculations based on the finite element methods (FEM). This approach results in a large number of degrees of freedom (DOFs) due to the discretization of the device geometry in finite element models, which has a significant drawback of long computational time. This is particularly pressing for modeling the transient behavior, but is also important when a large number of static cases are needed for optimization. For system-level designers to have computationally efficient models, it is necessary to develop reduced-order models that can be implemented by *e.g.* using MATLAB or a circuit simulator yet faithfully representing the device physics.

System-level models can be made few DOFs through model-order-reduction (MOR) techniques.[9] These techniques aim for an efficient projection to eliminate several DOFs and maintain the ones sufficient to capture the system behavior. However, such an approach hinges on first solving a model with many DOFs, then reducing. The MOR approach solves the problem of obtaining a low order system-level model, but still requires a significant computational effort to obtain it. Therefore, it is of interest to have methods that, unlike the MOR techniques, give a low order model directly without relying on projection.

Low order models can in principle be obtained by analytical or semi-analytical (series expansion) solutions. For similar mechanical problems of a rectangular plate with a circular hole, which is a common substructure in naval and aircraft architectures, this can be done.[10,11] However, these solutions are not applicable to the lens because the problems are different. In particular, the lens has additional physics due to the piezoelectric film and does not have a hole, but a circular purely elastic region instead.

To evaluate the linear static performance of piezoelectrically actuated lenses, we previously es-

tablished a modeling framework[12] composed of two parts. The first part is a variational formulation that models the lens' deformation due to piezoelectric actuation while the second part evaluates the lens' optical parameters such as the F-number ($F\#$) and RMS-wavefront-error (RMSWFE). We represented the diaphragm deflection by an expansion in a weighted Gegenbauer basis[12] using a formulation similar to,[13] but including piezoelectricity and the elasticity of the circular part. In this case, each basis function is extended continuously over the entire diaphragm and 120 DOFs were necessary to reach a satisfactory representation of the lens optical performance. While this is a major improvement in computational effort compared to FEM, it is still a quite large number of DOFs for lumped-model system simulations and too large to be tractable by purely analytical means.

One weakness in the previous formulation was that the basis functions did not account for the discontinuity of the layered structure at the lens opening. There are good reasons to expect that an improvement in convergence could be achieved by taking this discontinuity into account. For example, the deflection of purely elastic circular plates due to asymmetric bending[14,15] was previously modeled using circular and annular FEM elements with analytical solutions of the biharmonic equation as interpolation functions instead of general ones such as hexahedral or tetrahedral elements. It improved convergence, reduced the requirements on mesh refinement and represented the curved boundary well.

Motivated by the previous solutions to the purely mechanical problem,[11,13–15] this paper presents an approach that signifcantly improves model accuracy for the piezoelectrically actuated lens by using basis functions that account for the discontinuity in the layered structure at the lens opening, uses the exact solution of the biharmonic equation in the circular regions and fulfills the boundary conditons at the diaphragm edges.

We have chosen analytical ansätze that have Gegenbauer-polynomial-based subfunctions with rectangular symmetry satisfying the plate's boundary conditions and yet can be expanded on the form of Fourier series along the circular discontinuity to be matched term-by-term with the exact solutions of the plate's differential equation. Thus, the presented models can be generally used for any similar structures after reformulating the variational formulation to include the actuating forces due to *e.g.* pressure, piezoelectricity or thermoelasticity. For our lens application, the approach succeeds in reducing the model down to 10 DOFs as opposed to 120 for the same accuracy in the previous approach.

2 Principle of Operation

The piezoelectrically actuated MEMS lens is composed of a refractive polymer sandwiched between two transparent glass layers and with a piezoelectric stack on top (see Fig. 1). The upper glass layer is bent upwards due to the piezoelectric coupling whenever a DC voltage V_{p} is applied across the piezoelectric stack. As a result, the soft polymer follows the plate deformation and forms a plano-convex lens focusing light rays. In this manner, the lens's focal length can be tuned using the voltage V_{p} in order to focus on objects at varying distances. This type of tunable lenses can be combined with a fixed-focal-length lens to tune the overall system focal length.

3 Normalized coordinates

The diaphragm of the considered lens is square with a side length a and is clamped along its four sides. Figure 2 shows planar views of the lens marked with definitions used by different models. Models 0 and 1 break the lens domain Ω into two subdomains Ω_1 and Ω_2 while model 2 breaks it into 3 subdomains Ω_{I}, Ω_{II} and Ω_{III} (we have assigned new labels for subdomains in model 2 to
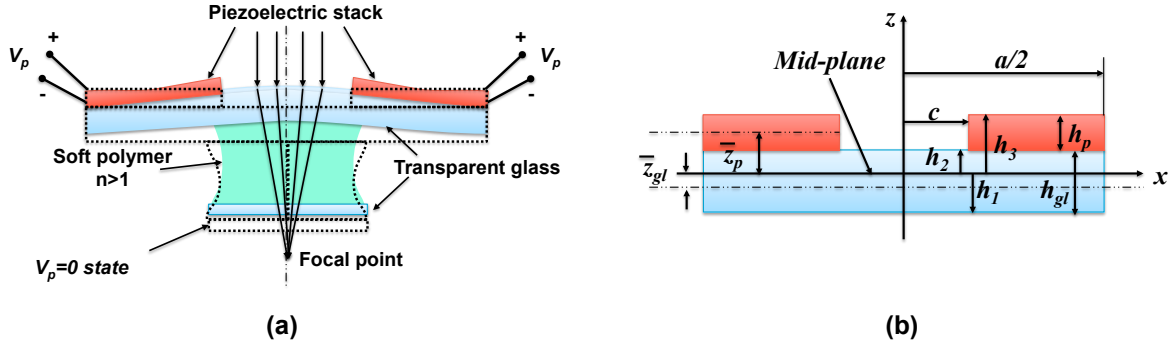
4

Fig 1 (a) Schematic view showing the tunable lens's principle of operation; both at rest position when $V_\mathrm{p} = 0$ and at focus when V_p is nonzero. (b) Cross-sectional view of the tunable lens showing dimensions. (Adapted with permission from Ref. 12, OSA).

simplify the mathematical representation of variables later on). The lens diaphragm extends over a square with cartesian coordinates $x, y \in [-a/2, a/2]$ and it is convenient to introduce normalized coordinates $X = 2x/a$ and $Y = 2y/a$. Thus, the locus of the lens pupil boundary (Γ_{Ω_1} in Fig. 2a or $\Gamma_{\Omega_\mathrm{I}}$ in Fig. 2b) and the fictitious boundary $\Gamma_{\Omega_\mathrm{II}}$ in these normalized cartesian coordinates are given by $\sqrt{X^2 + Y^2} = \gamma_1$ and $\sqrt{X^2 + Y^2} = \gamma_2$ where γ_1 and γ_2 respectively are the ratio of the lens pupil and the fictitious circle diameters to the diaphragm side length a.

The lens' circular and annular subdomains Ω_1, Ω_I and Ω_II can be further normalized to a radial coordinate, as shown in Fig. 3. For these subdomains, we use the normalized radial coordinate $r = \sqrt{X^2 + Y^2}/\gamma_0$ with $\gamma_0 = \gamma_1$ for models 0 and 1 and to $\gamma_0 = \gamma_2$ for model 2. As shown in Fig. 3, the lens pupil boundary for the different models is either of the circles $r = 1$ or $r = \alpha$ where $\alpha = \gamma_1/\gamma_2$.

4 Variational formulation and its integrals

We use the variational formulation formerly presented in Ref. 12. It is based on classical laminated plate theory, linear piezoelectricity, quasi-electrostatic conditions and thin film approximation. The lens thickness is much smaller than its lateral dimension which justifies applying the classical
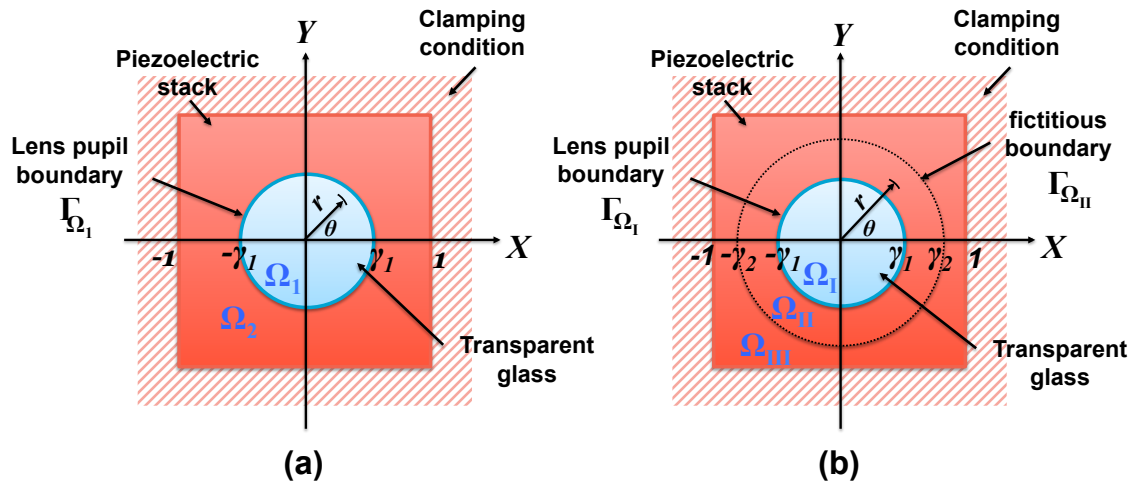
Fig 2 Planar views of the piezoelectrically actuated MEMS tunable lens showing decomposing its structure into subdomains. (a) Models 0 and 1 break the lens into two subdomains: Ω_1 and Ω_2. (b) Model 2 breaks it into three subdomains: Ω_I, Ω_{II} and Ω_{III}. Subdomains Ω_{II} and Ω_{III} are separated by a fictitious circular boundary $\Gamma_{\Omega_{II}}$.
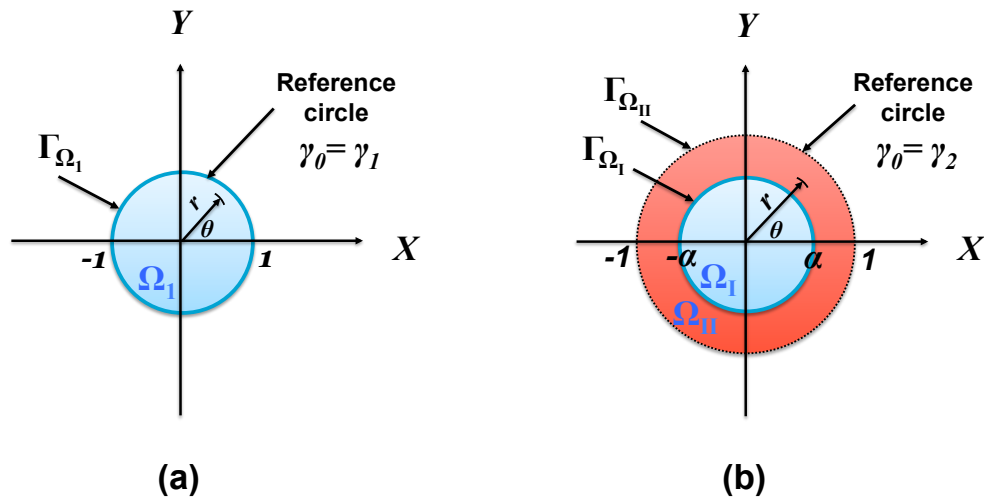

Fig 3 Planar views showing the normalized radial coordinates in the circular and annular subdomains for (a) models 0 and 1, and (b) model 2.

laminated plate theory.[16] Thus, the model assumes that the deflection in z-direction w_0 is due to bending and shear strains are neglected. The middle-plane stretching and the corresponding axial in-plane displacements are also neglected.

For a piezoelectric medium,[17] the principle of virtual work can be stated as

$$\delta H - \delta W = 0 \tag{1}$$

where δH is the virtual variation of the electrical enthalpy $H = H(\{S_{ij}\}, \{E_k\})$ and δW is the virtual variation of potential energy due to external applied forces. S_{ij} and E_k are components of strain and the electric field. The displacements in strain expressions are usually approximated by ansatz (discussed thoroughly in section 5) that is a linear combination of basis functions whose weights are to be determined. Equation (1), after substituting a displacement ansatz, is can be expressed as

$$\sum_q R_{\Omega_q} - \sum_q F_{\Omega_q} = 0 \tag{2}$$

where R_{Ω_q} and F_{Ω_q} are the spring and force variational energy integrals for the subdomain Ω_q. We will write these integrals on general forms to simplify the later presentation of the variational formulation of the three models in section 5. These general forms have arguments representing geometry, material parameters and displacement ansatz for each subdomain. Thus, the spring variational integrals over square (subscript □) and annular (or circular, subscript ○) subdomains can be written as

$$R_\square(w_0, \delta w_0; \mathbf{D}^*) = \frac{1}{(a/2)^2} \int_{-1}^{1} \int_{-1}^{1} \mathbf{U}^T \mathbf{D}^* \delta \mathbf{U} \mathrm{d}X \mathrm{d}Y, \tag{3}$$

$$R_\circ(w_0, \delta w_0; \mathbf{D}^*, \gamma_0, \alpha_H, \alpha_L) =$$

$$\frac{1}{\gamma_0^2 (a/2)^2} \int_{\alpha_L}^{\alpha_H} \int_0^{2\pi} \mathbf{V}^T \mathbf{D}^* \delta \mathbf{V} r \mathrm{d}r \mathrm{d}\theta \tag{4}$$

where

$$\mathbf{U} = \begin{bmatrix} w_{0,XX} \\ w_{0,YY} \\ 2w_{0,XY} \end{bmatrix}, \mathbf{V} = \begin{bmatrix} w_{0,rr} \\ \left(\frac{1}{r} w_{0,r} + \frac{1}{r^2} w_{0,\theta\theta} \right) \\ 2 \left(\frac{1}{r} w_{0,r\theta} - \frac{1}{r^2} w_{0,\theta} \right) \end{bmatrix}. \tag{5}$$

$\alpha_L, \alpha_H \in [0, 1]$ represent the lower and upper limits for the integral over the normalized coordinate r for an annular (or circular) subdomain. The modified membrane flexural rigidity matrix is defined as

$$\mathbf{D}^* = \begin{bmatrix} D_{11}^* & D_{12}^* & 0 \\ D_{12}^* & D_{22}^* & 0 \\ 0 & 0 & D_{66}^* \end{bmatrix}. \tag{6}$$

The modified flexural rigidities for each subdomain varies due to the difference in layer struc-

tures. For the tunable lens under study we have

$$\textbf{Models 0 \& 1:}\quad D^*_{ij,\Omega_1} = D^{\text{gl}}_{ij},$$

$$D^*_{ij,\Omega_2} = D^{\text{gl}}_{ij} + D^{\text{p}}_{ij},$$

$$\textbf{Model 2:}\quad D^*_{ij,\Omega_{\text{I}}} = D^{\text{gl}}_{ij},$$

$$D^*_{ij,\Omega_{\text{II}}} = D^*_{ij,\Omega_{\text{III}}} = D^{\text{gl}}_{ij} + D^{\text{p}}_{ij}$$

where D^{gl}_{ij} and D^{p}_{ij} are respectively the flexural rigidities for the glass layer only and the piezoelectric layer only.

The force variational energy integrals over square and annular subdomains can be written as

$$F_\square(\delta w_0) = V_{\text{p}}\overline{z}_{\text{p}}\overline{e}_{31} \int_{-1}^{1}\int_{-1}^{1} \nabla^2\delta w_0 \mathrm{d}X\mathrm{d}Y$$

$$= V_{\text{p}}\overline{z}_{\text{p}}\overline{e}_{31} \oint_{\Gamma_\Omega} \nabla\delta w_0 \cdot \mathrm{d}\hat{\mathbf{n}} = 0, \tag{7}$$

$$F_\circ(\delta w_0; \alpha_H, \alpha_L) = V_p\overline{z}_p\overline{e}_{31} \int_{\alpha_L}^{\alpha_H}\int_{0}^{2\pi} \nabla^2\delta w_0 r\mathrm{d}r\mathrm{d}\theta \tag{8}$$

where $\overline{z}_p = (h_3 + h_2)/2$ (see Fig. 1b) and $\overline{e}_{31}$ is the effective longitudinal e-form piezoelectric coupling coefficient.[12] The 2-D Laplace operator ∇^2 can be expressed in normalized cartesian or polar coordinates according to the shape of the domain. $\mathrm{d}\hat{\mathbf{n}}$ is the differential length vector normal to the lens outer boundary Γ_Ω. Using Green's theorem, we have written the surface integral in Eq. (7) as a line integral over the closed boundary Γ_Ω. The displacement anstaz inside that integral must satisfy the lens clamping conditions of zero slope along the four membrane sides, which

9

mandates Eq. (7) to be always equal to 0.

5 Models

This section describes mathematically the basis functions in the lens subdomains and the linear system of equations that arises from the variational formulation for three models. In order to have a good representation in each subdomain, different functional forms can be used in each domain. For each subdomain, the displacement is specified as a subfunction that is a linear combination of basis functions that are specific to the domain. The subfunctions in neighboring subdomains are required to satisfy continuity of displacement, slope and, if needed, higher derivatives of displacement. Hence, the coefficients of the different subfunctions are not independent degrees of freedom. Instead, the coefficents of the inner domain(s) can be expressed uniquely in terms of the coefficients of the outer domain.

Ideally, the number of basis functions (or number of DOFs) should be infinite to span any displacement. However, the variational models use a finite number of these functions, which form a finite subspace of this infinitely-sized space.[18] The dimension of this finite subspace is increased to improve accuracy of the predicted mechanical and optical quantities.

In the following analysis due to lens mirror symmetries, we will only consider 4-fold symmetric trial functions from Gegenbauer polynomials and the homogeneous solution of the plate differential equations to be displacement ansatz.

5.1 Model 0

This model from[12] uses weighted Gegenbauer polynomials as basis functions over all the lens planar subdomains. These polynomials do not satisfy the plate differential equations, but they sat-

isfy the clamped boundary conditions of zero displacement and slope along the square diaphragm edges. Moreover, they are orthogonal polynomials and are easily mapped to Zernike polynomials[12] which are suitable for optical wavefornt representation. With these basis functions, 120 independent DOFs were needed to obtain a satisfying representation of the lens's optical performance from this variational model when compared to FEM simulations.[12,19]

5.1.1 Weighted Gegenbauer Polynomials

These basis functions are orthogonal functions in the normalized variables X and Y. They are products of a weight factor $(X^2 - 1)^2(Y^2 - 1)^2$ and two Gegenbauer polynomials; one is a function of X and the other a function of Y. The weight factor enforces zero displacement and slope along the square membrane edges. A function in the basis is conveniently denoted ϕ_{lj} where the first index denotes the X-dependent Gegenbauer polynomial and the second one denotes the Y-dependent polynomial. Due to the 90° rotational symmetry of the lens structure, not all combinations of basis functions are possible. We can reduce the basis to a single-index set of functions Φ_k given by

$$\Phi_k(X, Y) = \frac{1}{2} \left[\phi_{lj}(X, Y) + \phi_{jl}(X, Y) \right] \tag{9}$$

where only *even* indices $l, j = 0, 2, \cdots N - 1$ occur; N is an odd number representing the number of Gegenbauer polynomials for either of the variables X or Y. The index $k = 1, 2, \cdots, N_G = \frac{1}{8}(N + 1)(N + 3)$ enumerates the single-index basis functions. The label k is obtained from the indices l, j by counting along the zigzag trajectory shown in Fig. 4. This simplification reduces the number of basis functions from $\frac{1}{4}(N + 1)^2$ to N_G which is nearly a factor 2 for large N values.
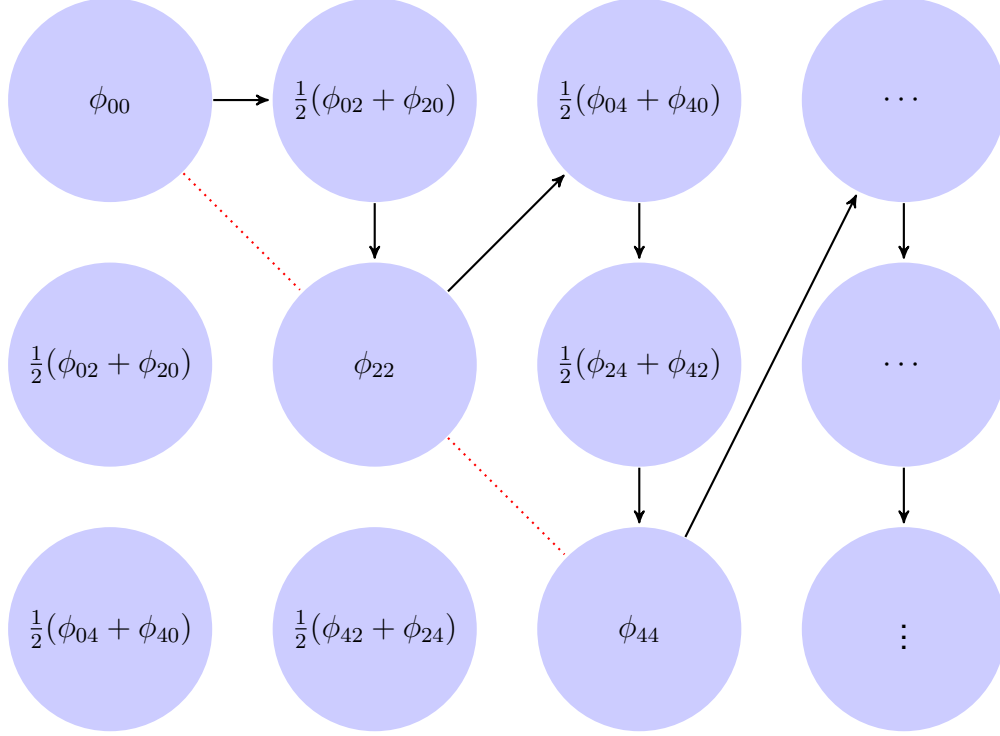
11

Fig 4 Zig-zag trajectory to obtain single-index Gegenbauer polynomials from the ones with double-index.

The first three Φ_k are

$$\Phi_1(X,Y) = \phi_{00} = (X^2 - 1)^2(Y^2 - 1)^2, \tag{10}$$

$$\Phi_2(X,Y) = \frac{1}{2}(\phi_{02} + \phi_{20})$$
$$= \frac{9}{4}\phi_{00}(11X^2 + 11Y^2 - 2), \tag{11}$$

$$\Phi_3(X,Y) = \phi_{22}$$
$$= \frac{81}{4}\phi_{00}(11X^2 - 1)(11Y^2 - 1). \tag{12}$$

For the lens' subdomains with circular symmetry, it is sometimes more convenient to use polar coordinates r and θ such that $(X,Y) = (\gamma_0 r \cos\theta, \gamma_0 r \sin\theta)$ and the basis functions are

$\widetilde{\Phi}_k(r, \theta, \gamma_0) = \Phi_k(\gamma_0 r \cos\theta, \gamma_0 r \sin\theta)$. Using MATLAB symbolic toolbox,[20] the first three $\widetilde{\Phi}_k$ are

$$\widetilde{\Phi}_1 = \frac{3}{128}\gamma_0^8 r^8 - \frac{1}{4}\gamma_0^6 r^6 + \frac{5}{4}\gamma_0^4 r^4 - 2\gamma_0^2 r^2 + 1$$
$$- \frac{1}{32}\gamma_0^4 r^4(\gamma_0^4 r^4 - 8\gamma_0^2 r^2 + 8)\cos(4\theta)$$
$$+ \frac{1}{128}\gamma_0^8 r^8 \cos(8\theta), \tag{13}$$

$$\widetilde{\Phi}_2 = \frac{9}{512}(11\gamma_0^2 r^2 - 2)\Big[(3\gamma_0^8 r^8 - 32\gamma_0^6 r^6 + 160\gamma_0^4 r^4$$
$$- 256\gamma_0^2 r^2 + 128)$$
$$- 2\gamma_0^4 r^4(\gamma_0^4 r^4 - 8\gamma_0^2 r^2 + 8)\cos(4\theta)$$
$$+ \gamma_0^8 r^8 \cos(8\theta)\Big], \tag{14}$$

$$\widetilde{\Phi}_3 = \frac{49005}{4096}\gamma_0^{12} r^{12} - \frac{61479}{512}\gamma_0^{10} r^{10} + \frac{244377}{512}\gamma_0^8 r^8$$
$$- \frac{14337}{16}\gamma_0^6 r^6 + \frac{24867}{32}\gamma_0^4 r^4 - \frac{1053}{4}\gamma_0^2 r^2 + \frac{81}{4}$$
$$- \frac{81}{8192}\gamma_0^4 r^4\Big(1815\gamma_0^8 r^8 - 16192\gamma_0^6 r^6$$
$$+ 52160\gamma_0^4 r^4 - 68096\gamma_0^2 r^2 + 31488\Big)\cos(4\theta)$$
$$+ \frac{81}{4096}\gamma_0^8 r^8\Big(363\gamma_0^4 r^4 - 2024\gamma_0^2 r^2$$
$$+ 1944\Big)\cos(8\theta) - \frac{9801}{8192}\gamma_0^{12} r^{12} \cos(12\theta). \tag{15}$$

From Eqs. (13-15), each basis function has the form of a Fourier cosine series that can be

expressed as

$$\Phi_k(X, Y) = \widetilde{\Phi}_k(r, \theta, \gamma_0) = f_{k,0}(r, \gamma_0)$$
$$+ \sum_{n=2,4,6\cdots}^{N_{s,k}} f_{k,n}(r, \gamma_0) \cos(n\theta) \qquad (16)$$

where n is the Fourier series index. $f_{k,n}(r, \gamma_0)$ is the nth Fourier coefficient for the function $\widetilde{\Phi}_k$ and is dependent on the normalized radial coordinate r and the ratio γ_0. Due to the lens' 4-fold symmetry, the coefficients $f_{k,n}(r, \gamma_0)$ with $n = 2, 6, 10, \cdots$ are zero. $N_{s,k}$ is the number of Fourier terms used to expand the function $\widetilde{\Phi}_k$.

To represent any basis function ϕ_{lj} by a Fourier series, the Fourier terms need to be up to $N_{s,lj} = l + j + 8$. Thus, the highest order in Fourier terms for a function set of N_G single-index Gegenbauer polynomials is $N_F = \max(N_{s,lj}) = 2(N - 1) + 8$. Table 1 shows examples of the corresponding number N_F and index k values for a certain number of Gegenbauer polynomials N. In that manner, a function set of N_G single-index basis functions form a finite Gegenbauer space $\mathbb{R}^{N_G}$ that can be mapped to a Fourier space $\mathbb{R}^{N_F/2+1}$ using Eq. (16).

Table 1 Examples on Gegenbauer polynomials order N with its correspondent values for the single index k and the number of sufficient Fourier terms N_F.

N	1	3	5	7	9
$k = 1 \rightarrow N_G$	1	1$\rightarrow$3	1$\rightarrow$6	1$\rightarrow$10	1$\rightarrow$15
$N_F = \max(N_{s,lj})$	8	12	16	20	24

Model 0 approximates the lens displacement with a finite linear combination of basis functions

14

$$\Phi_k(X,Y)$$

$$
\begin{aligned}
w_0(X,Y) = \widetilde{w}_0(r,\theta,\gamma_0) &= \sum_{k=1}^{N_G} C_k \Phi_k(X,Y) \\
&= \sum_{k=1}^{N_G} C_k \widetilde{\Phi}_k(r,\theta,\gamma_0)
\end{aligned}
\tag{17}
$$

where C_k are the coefficients to be determined.

5.1.2 Variational formulation

After substituting with the displacement ansatz from Eq. (17) in the variational formulation of Eq. (2), it becomes

$$R_{\Omega_1} + R_{\Omega_2} = F_{\Omega_1} + F_{\Omega_2}. \tag{18}$$

such that

$$R_{\Omega_1} = R_\circ(w_0, \delta w_0; \mathbf{D}^*_{\Omega_1}, \gamma_1, 1, 0) = \delta\mathbf{C}^T \mathbf{R}^{\Omega_1}_{k_1 k_2} \mathbf{C}, \tag{19}$$

$$
\begin{aligned}
R_{\Omega_2} &= R_\square(w_0, \delta w_0; \mathbf{D}^*_{\Omega_2}) \\
&\quad - R_\circ(w_0, \delta w_0; \mathbf{D}^*_{\Omega_1}, \gamma_1, 1, 0) = \delta\mathbf{C}^T \mathbf{R}^{\Omega_2}_{k_1 k_2} \mathbf{C},
\end{aligned}
\tag{20}
$$

$$F_{\Omega_1} = 0, \tag{21}$$

$$F_{\Omega_2} = F_\square(\delta w_0) - F_\circ(\delta w_0, 1, 0) = \delta\mathbf{C}^T \mathbf{F}_{k_2}, \tag{22}$$

where $\mathbf{C}$ is a column vector of the DOFs C_k. Expressions of the elements in the matrices $\mathbf{R}^{\Omega_q}_{k_1 k_2}$ ($q = 1, 2$) and $\mathbf{F}_{k_2}$ are listed in Appx. A. The planar subdomain Ω_2 is prismatic and can be imagined to result from subtracting a domain with a circular base face from another one with a

15

square base face (see Fig. 2a). From that aspect, integrals over that subdomain are easily calculated as a difference between two integrals as in Eqs. (20) and (22); the first is over a square area and the second is over a circular area.

By combining the variational terms from Eqs. (19-22) and substitute in Eq. (18), model-0's variational formulation turns to be

$$\delta\mathbf{C}^T\left(\mathbf{R}_{k_1k_2}^{\Omega_1} + \mathbf{R}_{k_1k_2}^{\Omega_2}\right)\mathbf{C} = \delta\mathbf{C}^T\mathbf{F}_{k_2}. \tag{23}$$

The above variational formulation is solved if the coefficient vector $\mathbf{C}$ is a non-trivial solution to the linear system of equations

$$\left(\mathbf{R}_{k_1k_2}^{\Omega_1} + \mathbf{R}_{k_1k_2}^{\Omega_2}\right)\mathbf{C} = \mathbf{F}_{k_2}. \tag{24}$$

Each term inside the parentheses on the left-hand side (LHS) represents the equivalent stiffness matrix of each lens subdomain. The right-hand side (RHS) represents the equivalent force due to the piezoelectric actuation.

5.2 Model 1

Model-1 deals with the lens as a 2-subdomains problem similar to model 0, but it uses a piecewise expansion of two different basis functions for the displacement approximation in the pupil and

actuator regions. Its displacement ansatz in the lens subdomains is

$$\Omega_1: \quad w_0^{(1)} = A_0^{\mathrm{I}} + B_0^{\mathrm{I}} r^2$$

$$+ \sum_{n=2,4,6\cdots}^{N_F} \left(A_n^{\mathrm{I}} r^n + B_n^{\mathrm{I}} r^{n+2} \right) \cos(n\theta), \tag{25}$$

$$\Omega_2: \quad w_0^{(2)} = \sum_{k=1}^{N_G} C_k \Phi_k(X, Y) \tag{26}$$

where $w_0^{(1)}$ is the subfunction of the displacement ansatz in the subdomain Ω_1. It has $N_L = N_F + 2$

coefficients A_i^{I} and B_i^{I} for $i = 0, 2, \cdots N_F$ to be determined. Due to the lens symmetry, $w_0^{(1)}$

has only even terms of the general homogeneous solution for the plate differential equation.[21]

To have a bounded solution at the origin $r = 0$, we have eliminated logarithmic and negative-

power terms from the homogeneous solution. Moreover, we have limited the upper value of the

summation index in Eq. (25) to N_F in order to have the same trigonometric terms as in the weighted

Gegenbauer basis from Eq. (26). This limitation follows from the continuity requirement on

the displacement and the slope at the boundary Γ_{Ω_1} separating the lens' subdomains (thoroughly

discussed in section 5.2.1). The ansatz part $w_0^{(1)}$ is equivalent to having a circular FEM element

with interpolation functions formed as a product of two polynomials: one is an even polynomial in

r for the radial direction and the other a cosine function for the circumferential direction.[15]

For the subdomain Ω_2, the subfunction $w_0^{(2)}$ is the same single-index Gegenbauer basis used in

model 0 to enforce the clamped boundary conditions.

5.2.1 *Relationships between coefficients at the pupil boundary Γ_{Ω_1}*

Both subfunctions of the ansatz in model 1 have the form of a Fourier series; sum of products

of a radial factor and a trigonometric function. The radial factor multiplying each trigonometric

function of $w_0^{(1)}$ has two coefficients while those of $w_0^{(2)}$ have only one coefficient. To find a relation between these two sets of coefficients at Γ_{Ω_1}, two boundary conditions are required: continuity of the displacement and of the slope. Hence, we equate the radial factor of trigonometric terms (term by term) of the pair $(w_0^{(1)}, w_{0,r}^{(1)})$ to their counterpart radial factor of the trigonometric terms of $(w_0^{(2)}, w_{0,r}^{(2)})$ at the boundary Γ_{Ω_1} where $\gamma_0 = \gamma_1$ and $r = 1$. In matrix form, the relation is compactly expressed as

$$\mathbf{L_I}|_{r=1}\mathbf{A_I} = \mathbf{N_I}\mathbf{C}$$

$$= \begin{bmatrix} \mathbf{N}_{1,\mathrm{I}} & \mathbf{N}_{2,\mathrm{I}} & \cdots & \mathbf{N}_{N_G,\mathrm{I}} \end{bmatrix} \begin{bmatrix} C_1 \\ C_2 \\ \vdots \\ C_{N_G} \end{bmatrix}. \tag{27}$$

where

$$\mathbf{L_I} = \begin{bmatrix} \mathbf{L}_{0,\mathrm{I}} & \mathbf{0} & \mathbf{0} & \cdots & \mathbf{0} \\ \mathbf{0} & \mathbf{L}_{2,\mathrm{I}} & \mathbf{0} & \cdots & \mathbf{0} \\ \vdots & & \ddots & & \mathbf{0} \\ \mathbf{0} & \mathbf{0} & \mathbf{0} & \cdots & \mathbf{L}_{N_F,\mathrm{I}} \end{bmatrix}, \tag{28}$$

$$
\mathbf{A}_\mathrm{I} = \begin{bmatrix} \mathbf{A}_{0,\mathrm{I}} \\ \\ \mathbf{A}_{2,\mathrm{I}} \\ \vdots \\ \\ \mathbf{A}_{N_F,\mathrm{I}} \end{bmatrix}, \quad \mathbf{A}_{i,\mathrm{I}} = \begin{bmatrix} A_i^\mathrm{I} \\ \\ B_i^\mathrm{I} \end{bmatrix} \tag{29}
$$

$$
\mathbf{N}_{k,\mathrm{I}} = \begin{bmatrix} \mathbf{N}_{k,0}^\mathrm{I} \\ \\ \mathbf{N}_{k,2}^\mathrm{I} \\ \vdots \\ \\ \mathbf{N}_{k,N_{s,k}}^\mathrm{I} \\ \\ \mathbf{0} \end{bmatrix}. \tag{30}
$$

In Eq. (27), the column vector $\mathbf{N}_{k,\mathrm{I}}$ of length N_L represents the radial factors and their derivatives of each basis function Φ_k. The index of Fourier terms for each function Φ_k ranges from 0 to $N_{s,k}$. Thus, the last $N_L - N_{s,k} - 2$ elements of the $\mathbf{N}_{k,\mathrm{I}}$ column are zeros while the first $N_{s,k} + 2$ ones can be calculated from Eq. (16). The submatrices of $\mathbf{L}_{i,\mathrm{I}}$ and $\mathbf{N}_{k,\mathrm{I}}$ are given by

$$
\mathbf{L}_{i,\mathrm{I}} = \begin{bmatrix} r^i & r^{i+2} \\ \\ ir^{i-1} & (i+2)r^{i+1} \end{bmatrix},
$$

$$
\mathbf{N}_{k,i}^I = \begin{bmatrix} f_{k,i}(r=1, \gamma_0 = \gamma_1) \\ \\ f_{k,i}'(r=1, \gamma_0 = \gamma_1) \end{bmatrix} \tag{31}
$$

where the prime in $f_{k,i}'$ denotes differentiation with respect to the variable r. Rows of the product $\mathbf{L}_{i,\mathrm{I}}\mathbf{A}_{i,\mathrm{I}}$ and $\sum_{k=1}^{N_G} \mathbf{N}_{k,i}^I C_k$ respectively correspond to i^{th}-radial factor of the trigonometric terms of

the pairs $(w_0^{(1)}, w_{0,r}^{(1)})$ in Eq. (25) and $(w_0^{(2)}, w_{0,r}^{(2)})$ in Eqs. (16) and (26).

Since $\mathbf{L}_I$ is a square invertible matrix, Eq. (27) can be rewritten as

$$\mathbf{A}_I = \mathbf{L}_I^{-1}|_{r=1}\mathbf{N}_I\mathbf{C} = \mathbf{T}_1\mathbf{C}, \quad \mathbf{T}_1 \in \mathbb{R}^{N_L \times N_G} \tag{32}$$

where $\mathbf{T}_1$ is model 1's transformation matrix relating coefficientss $\mathbf{A}_I$ and $\mathbf{C}$ in the adjacent sub-domains. Appendix B lists an example of the matrices $\mathbf{T}_1$ and $\mathbf{N}_I$ using the first basis function Φ_1. To numerically calculate $\mathbf{L}_I^{-1}$, we use the analytic expression of the inverse of submatrices $\mathbf{L}_{i,I}^{-1}$ from Eq. (72) in Appx. B. The determinant of the matrix $\mathbf{L}_I$, given by,

$$\det \mathbf{L}_I = \prod_{i=0,\cdots\text{even}}^{N_L} \det \mathbf{L}_{i,I} = \prod_{i=0,\cdots\text{even}}^{N_L} r^{i+1} \tag{33}$$

strongly depends on the value of r at the pupil boundary. The determinant will not form a numerically ill-conditioned problem for model 1 since $r = 1$ at the boundary. However, this is not the case for model 2 that also uses Eq. (32) but with $r = \alpha, \alpha < 1$ (see section 5.3.1).

5.2.2 Variational formulation

Model 1 has the same variational terms as model 0, after replacing w_0 with $w_0^{(2)}$, except for the term in Eq. (19). This term is modified to

$$R_{\Omega_1} = R_\circ(w_0^{(1)}, \delta w_0^{(1)}; \mathbf{D}_{\Omega_1}^*, \gamma_1, 1, 0)$$

$$= \delta \mathbf{A}_I^T \mathbf{H}^{\Omega_1} \mathbf{A}_I \tag{34}$$

20

where $\mathbf{H}^{\Omega_1}$ is obtained from $\mathbf{H}^{\Omega_q}$ defined in appx. C after extracting only the upper left quadrants from its submatrices $\mathbf{H}_i^{\mathrm{I}_m}$ and setting $r = 1$.

Using Eqs. (20-22), (32) and (34), the linear system of equations to is modified to be

$$\left(\mathbf{T}_1^T \mathbf{H}^{\Omega_1} \mathbf{T}_1 + \mathbf{R}_{k_1 k_2}^{\Omega_2}\right) \mathbf{C} = \mathbf{F}_{k_2} \tag{35}$$

where the first term inside the parentheses in the LHS represents the stiffness of subdomain Ω_1 using the new subfunction $w_0^{(1)}$.

5.3 Model 2

Model 2 deals with the lens as a 3-subdomains problem (refer to Fig. 2b). To further improve the model accuracy over model 1 at low DOFs, this model enlarges the membrane area over which the homogeneous solution of the plate equation is used beyond the pupil area. Therefore, it adds a fictitious boundary $\Gamma_{\Omega_{\mathrm{II}}}$ that amounts to having a new annular subdomain Ω_{III}. Its displacement ansatz in the lens subdomains becomes

$$\Omega_{\mathrm{I}}\colon \quad w_0^{(\mathrm{I})} = A_0^{\mathrm{I}} + B_0^{\mathrm{I}} r^2$$

$$+ \sum_{n=2,4,6,\cdots}^{N_F} \left(A_n^{\mathrm{I}} r^n + B_n^{\mathrm{I}} r^{n+2}\right) \cos(n\theta), \tag{36}$$

$$\Omega_{\mathrm{II}}\colon \quad w_0^{(\mathrm{II})} = A_0^{\mathrm{II}} + B_0^{\mathrm{II}} r^2 + C_0^{\mathrm{II}} \ln(r) + D_0^{\mathrm{II}} r^2 \ln(r)$$

$$+ \sum_{n=2,4,6,\cdots}^{N_F} \left(A_n^{\mathrm{II}} r^n + B_n^{\mathrm{II}} r^{n+2}\right.$$

$$\left. + C_n^{\mathrm{II}} r^{-n} + D_n^{\mathrm{II}} r^{-n+2}\right) \cos(n\theta), \tag{37}$$

$$\Omega_{\mathrm{III}}\colon \quad w_0^{(\mathrm{III})} = \sum_{k=1}^{N_G} C_k \Phi_k(X, Y) \tag{38}$$

where $w_0^{(\text{II})}$ is the subfunction of the displacement ansatz over the new annular subdomain Ω_{II} and has $2N_L$ coefficients to be determined. Its coefficients are A_i^{II}, B_i^{II}, C_i^{II} and D_i^{II} where $i = 0, 2, \cdots N_F$. $w_0^{(\text{II})}$ uses even terms of the full homogeneous solution to the plate equation including logarithmic and negative-power terms because the subdomain Ω_{II} does not enclose the origin. To maximize the membrane area over which $w_0^{(\text{II})}$ is used, we have chosen the fictitious circle's ratio $\gamma_2 = 1$ in the model-2's computation in section 5. This choice means that the homogeneous solution is used over the area of the inscribed circle of the square diaphragm. The subfunction $w_0^{(\text{II})}$ is equivalent to having an annular FEM element similar to.[15]

The subfunction $w_0^{(\text{I})}$ is used for the pupil subdomain as in model 1 while $w_0^{(\text{III})}$ is used over the subdomain Ω_{III} to enforce the clamped conditions, as discussed earlier.

5.3.1 Relationships between coefficients at the boundaries $\Gamma_{\Omega_{\text{I}}}$ and $\Gamma_{\Omega_{\text{II}}}$

Model 2 has two internal boundaries $\Gamma_{\Omega_{\text{I}}}$ and $\Gamma_{\Omega_{\text{II}}}$ at which we will formulate two relationships between coefficients of the subfunctions in adjacent subdomains in a similar way to the procedure followed for model 1.

The first relationship relates coefficients of $w_0^{(\text{III})}$ and $w_0^{(\text{II})}$. The radial factor of each trigonometric term of $w_0^{(\text{II})}$ has four coefficients while those of $w_0^{(\text{III})}$ have only one coefficient. Thus, to have a one-to-one relation between these two set of coefficients, we will need four boundary conditions at $\Gamma_{\Omega_{\text{II}}}$. Two of them are the continuities of displacement and slope. The other two are the continuities of radial moment M_{rr} and the vertical shear force Q_r. Since the boundary $\Gamma_{\Omega_{\text{II}}}$ is fictitious and there is no difference in layer structures, we have found that these later continuity conditions are essentially the same as having the 2nd and the 3rd derivatives of the displacement continuous (proven in Appx. D). Thus, the relationship can lastly be formulated by setting radial

factors of the trigonometric terms (term by term) of the mechanical quartet ($w_0^{(\text{III})}$, $w_{0,r}^{(\text{III})}$, $w_{0,rr}^{(\text{III})}$, $w_{0,rrr}^{(\text{III})}$) equal to their counterpart radial factors of ($w_0^{(\text{II})}$, $w_{0,r}^{(\text{II})}$, $w_{0,rr}^{(\text{II})}$, $w_{0,rrr}^{(\text{II})}$). This procedure is carried out for the fictitious boundary $\Gamma_{\Omega_{\text{II}}}$ where $\gamma_0 = \gamma_2$ and $r = 1$. In matrix form, the first relationship between coefficients is compactly expressed as

$$\mathbf{L}_{\text{II}}|_{r=1}\mathbf{A}_{\text{II}} = \mathbf{N}_{\text{II}}\mathbf{C}$$

$$= \begin{bmatrix} \mathbf{N}_{1,\text{II}} & \mathbf{N}_{2,\text{II}} & \cdots & \mathbf{N}_{N_G,\text{II}} \end{bmatrix} \begin{bmatrix} C_1 \\ C_2 \\ \vdots \\ C_{N_G} \end{bmatrix} \tag{39}$$

where

$$\mathbf{L}_{\text{II}} = \begin{bmatrix} \mathbf{L}_{0,\text{II}} & \mathbf{0} & \mathbf{0} & \cdots & \mathbf{0} \\ \mathbf{0} & \mathbf{L}_{2,\text{II}} & \mathbf{0} & \cdots & \mathbf{0} \\ \vdots & & \ddots & & \mathbf{0} \\ \mathbf{0} & \mathbf{0} & \mathbf{0} & \cdots & \mathbf{L}_{N_F,\text{II}} \end{bmatrix}, \tag{40}$$

$$\mathbf{A}_{\text{II}} = \begin{bmatrix} \mathbf{A}_{0,\text{II}} \\ \mathbf{A}_{2,\text{II}} \\ \vdots \\ \mathbf{A}_{N_F,\text{II}} \end{bmatrix}, \quad \mathbf{A}_{i,\text{II}} = \begin{bmatrix} A_i^{\text{II}} \\ B_i^{\text{II}} \\ C_i^{\text{II}} \\ D_i^{\text{II}} \end{bmatrix} \tag{41}$$

$$
\mathbf{N}_{k,\mathrm{II}} = \begin{bmatrix} \mathbf{N}^{\mathrm{II}}_{k,0} \\[6pt] \mathbf{N}^{\mathrm{II}}_{k,2} \\[6pt] \vdots \\[6pt] \mathbf{N}^{\mathrm{II}}_{k,N_L} \\[6pt] \mathbf{0} \end{bmatrix}. \tag{42}
$$

In Eq. (39), the column vector $\mathbf{N}_{k,\mathrm{II}}$ of length $2N_L$ represents the radial factors and their derivatives for the basis function Φ_k. The last $2N_L - 2N_{s,k} - 4$ elements of the $\mathbf{N}_{k,\mathrm{II}}$ column are zeros while the first $2N_{s,k} + 4$ ones can be calculated from Eq. (16). The submatrices $\mathbf{L}_{0,\mathrm{II}}$, $\mathbf{L}_{n,\mathrm{II}}$ and $\mathbf{N}^{\mathrm{II}}_{k,n}$ are given by

$$
\mathbf{L}_{0,\mathrm{II}} = \begin{bmatrix} 1 & r^2 & \ln(r) & r^2 \ln(r) \\[6pt] 0 & 2r & 1/r & r(2\ln(r)+1) \\[6pt] 0 & 2 & -1/r^2 & (2\ln(r)+3) \\[6pt] 0 & 0 & 2/r^3 & 2/r \end{bmatrix}, \tag{43}
$$

$$
\mathbf{L}_{n,\mathrm{II}} =
\begin{bmatrix}
r^n & r^{n+2} \\[6pt]
n^{\underline{1}} r^{n-1} & (n+2)^{\underline{1}} r^{n+1} \\[6pt]
n^{\underline{2}} r^{n-2} & (n+2)^{\underline{2}} r^n \\[6pt]
n^{\underline{3}} r^{n-3} & (n+2)^{\underline{3}} r^{n-1}
\end{bmatrix}
$$

$$
\begin{matrix}
r^{-n} & r^{2-n} \\[6pt]
(-n)^{\underline{1}} r^{-n-1} & (2-n)^{\underline{1}} r^{1-n} \\[6pt]
(-n)^{\underline{2}} r^{-n-2} & (2-n)^{\underline{2}} r^{-n} \\[6pt]
(-n)^{\underline{3}} r^{-n-3} & (2-n)^{\underline{3}} r^{-n-1}
\end{matrix}
\Bigg], \tag{44}
$$

$$
\mathbf{N}_{k,n}^{\mathrm{II}} =
\begin{bmatrix}
f_{k,n}(r=1, \gamma_0 = \gamma_2) \\[6pt]
f'_{k,n}(r=1, \gamma_0 = \gamma_2) \\[6pt]
f''_{k,n}(r=1, \gamma_0 = \gamma_2) \\[6pt]
f'''_{k,n}(r=1, \gamma_0 = \gamma_2)
\end{bmatrix}, \tag{45}
$$

where $n^{\underline{m}} = n(n-1)\cdots(n-m+1)$.

It is evident that rows of the product $\mathbf{L}_{i,\mathrm{II}}\mathbf{A}_{i,\mathrm{II}}$ and $\sum_{k=1}^{N_G} \mathbf{N}_{k,i}^{\mathrm{II}} C_k$ respectively correspond to the ith-radial factor of the trigonometric terms of the quartets $(w_0^{(\mathrm{II})}, w_{0,r}^{(\mathrm{II})}, w_{0,rr}^{(\mathrm{II})}, w_{0,rrr}^{(\mathrm{II})})$ from Eq. (37) and $(w_0^{(\mathrm{III})}, w_{0,r}^{(\mathrm{III})}, w_{0,rr}^{(\mathrm{III})}, w_{0,rrr}^{(\mathrm{III})})$ from Eqs. (16) and (38).

The second relationship relates coefficients of $w_0^{(I)}$ and $w_0^{(II)}$. Each trigonometric term of $w_0^{(\mathrm{II})}$ has four coefficients while those of $w_0^{(\mathrm{II})}$ have only two coefficients. Thus, to have a one-to-one relation between these two set of coefficients, two conditions are sufficient. The relationship is determined from the continuity of displacement and slope at the boundary $\Gamma_{\Omega_{\mathrm{I}}}$ where $r = \alpha =$

γ_1/γ_2. It can be expressed as

$$\mathbf{L}_{\mathrm{I}}|_{r=\alpha}\mathbf{A}_{\mathrm{I}} = \mathbf{L}^*{}_{\mathrm{II}}|_{r=\alpha}\mathbf{A}_{\mathrm{II}} \tag{46}$$

where $\mathbf{L}_{\mathrm{I}}$ and $\mathbf{A}_{\mathrm{I}}$ are defined in Eqs. (28) and (29). $\mathbf{L}^*{}_{\mathrm{II}}$ is obtained from $\mathbf{L}_{\mathrm{II}}$ by extracting only the upper left quadrant of the submatrices $\mathbf{L}_{i,\mathrm{II}}$ since the continuity of displacement and slope are enough to determine the relation between coefficients of $w_0^{(I)}$ and $w_0^{(II)}$. Using Eqs. (39) and (46), it is more convenient to express $\mathbf{A}_{\mathrm{II}}$ and $\mathbf{A}_{\mathrm{I}}$ in terms of the vector $\mathbf{C}$ as in

$$\mathbf{A}_{\mathrm{II}} = \mathbf{L}_{\mathrm{II}}^{-1}|_{r=1}\mathbf{N}_{\mathrm{II}}\mathbf{C} = \mathbf{T}_{\mathrm{II}}\mathbf{C}, \quad \mathbf{T}_{\mathrm{II}} \in \mathbb{R}^{2N_L \times N_G}, \tag{47}$$

$$\mathbf{A}_{\mathrm{I}} = \mathbf{L}_{\mathrm{I}}^{-1}|_{r=\alpha}\mathbf{L}^*{}_{\mathrm{II}}|_{r=\alpha}\mathbf{L}_{\mathrm{II}}^{-1}|_{r=1}\mathbf{N}_{\mathrm{II}}\mathbf{C}$$

$$= \mathbf{T}_{\mathrm{I}}\mathbf{C}, \quad \mathbf{T}_{\mathrm{I}} \in \mathbb{R}^{N_L \times 2N_L} \tag{48}$$

where $\mathbf{T}_{\mathrm{II}}$ and $\mathbf{T}_{\mathrm{I}}$ are model 2's transformation matrices. Appendix E lists an example of the matrices $\mathbf{N}_{\mathrm{II}}$, $\mathbf{T}_{\mathrm{II}}$ and $\mathbf{T}_{\mathrm{I}}$ using the first polynomial Φ_1. We calculate the transformation matrices using the analytic expression for the inverses. $\mathbf{L}_{\mathrm{II}}^{-1}$ is calculated from Eqs. (85) and (86) in Appx. E while $\mathbf{L}_{\mathrm{I}}^{-1}$ is calculated in the same procedure as discussed for model 1. The determinant of matrices $\mathbf{L}_{\mathrm{II}}$ given by

$$\det \mathbf{L}_{\mathrm{II}} = \det \mathbf{L}_{0,\mathrm{II}} \times \prod_{n=2,\cdots,\mathrm{even}}^{N_F} \det \mathbf{L}_{n,\mathrm{II}}$$

$$= \left(-16r^{-2}\right) \prod_{n=2,\cdots,\mathrm{even}}^{N_F} 64(n^4 - n^2)r^{-2} \tag{49}$$

strongly depends on the variables n and r. The higher the values of n, the more likely that we face

numerically ill-conditioned matrices when solving for the $\mathbf{C}$ vector. However, this can be dodged

by scaling the equivalent stiffness matrix and the vector $\mathbf{C}$ with a diagonal matrix (see section 6.1).

5.3.2 Variational formulation

With three subdomains, the variational formulation of Eq. (2) becomes

$$R_{\Omega_I} + R_{\Omega_{II}} + R_{\Omega_{III}} = F_{\Omega_I} + F_{\Omega_{II}} + F_{\Omega_{III}} \tag{50}$$

where

$$R_{\Omega_I} = R_\circ(w_0^{(I)}, \delta w_0^{(I)}; \mathbf{D}_{\Omega_I}^*, \gamma_2, \alpha, 0)$$

$$= \delta \mathbf{A}_I^T \mathbf{H}^{\Omega_I} \mathbf{A}_I = \delta \mathbf{C}^T \mathbf{T}_I^T \mathbf{H}^{\Omega_I} \mathbf{T}_I \mathbf{C}, \tag{51}$$

$$R_{\Omega_{II}} = R_\circ(w_0^{(II)}, \delta w_0^{(II)}; \mathbf{D}_{\Omega_{II}}^*, \gamma_2, 1, \alpha)$$

$$= \delta \mathbf{A}_{II}^T \mathbf{H}^{\Omega_{II}} \mathbf{A}_{II} = \delta \mathbf{C}^T \mathbf{T}_{II}^T \mathbf{H}^{\Omega_{II}} \mathbf{T}_{II} \mathbf{C}, \tag{52}$$

$$R_{\Omega_{III}} = R_\square(w_0^{(III)}, \delta w_0^{(III)}; \mathbf{D}_{\Omega_{III}}^*)$$

$$\quad - R_\circ(w_0^{(III)}, \delta w_0^{(III)}; \mathbf{D}_{\Omega_{III}}^*, \gamma_2, 1, 0)$$

$$= \delta \mathbf{C}^T \mathbf{R}_{k_1 k_2}^{\Omega_{III}} \mathbf{C}, \tag{53}$$

$$F_{\Omega_I} = 0, \tag{54}$$

$$F_{\Omega_{II}} = F_\circ(\delta w_0^{(II)}, 1, \alpha) = \delta \mathbf{A}_{II}^T \mathbf{F}_{II} = \delta \mathbf{C}^T \mathbf{T}_{II}^T \mathbf{F}_{II}, \tag{55}$$

$$F_{\Omega_{III}} = F_\square(\delta w_0^{(III)}) - F_\circ(\delta w_0^{(III)}, 1, 0) = \delta \mathbf{C}^T \mathbf{F}_{k_2}. \tag{56}$$

Expressions for the matrices $\mathbf{R}_{k_1 k_2}^{\Omega_{III}}$, $\mathbf{F}_{k_2}$ and $\mathbf{F}_{II}$ can be found in Appx. A and C. $\mathbf{H}^{\Omega_I}$ is obtained

from $\mathbf{H}^{\Omega_q}$ defined in Appx. C by extracting the upper left quadrants of its submatrices $\mathbf{H}_i^{\Omega_I}$ and

27

setting $r = \alpha$. $\mathbf{H}^{\Omega_{\mathrm{II}}}$ is related to the matrix $\mathbf{H}^{\Omega_q}$ by

$$\mathbf{H}^{\Omega_{\mathrm{II}}} = \mathbf{H}^{\Omega_q}\big|_{r=1} - \mathbf{H}^{\Omega_q}\big|_{r=\alpha}. \tag{57}$$

After collecting the variational terms, we acquire the following linear system of equations

$$\left(\mathbf{T}_{\mathrm{I}}^T \mathbf{H}^{\Omega_{\mathrm{I}}} \mathbf{T}_{\mathrm{I}} + \mathbf{T}_{\mathrm{II}}^T \mathbf{H}^{\Omega_{\mathrm{II}}} \mathbf{T}_{\mathrm{II}} + \mathbf{R}_{k_1 k_2}^{\Omega_{\mathrm{III}}}\right)\mathbf{C}$$
$$= \mathbf{T}_{\mathrm{II}}^T \mathbf{F}_{\mathrm{II}} + \mathbf{F}_{k_2}. \tag{58}$$

Each term inside the parentheses in the LHS of the above equation represents the equivalent stiffness matrix for a subdomain using the specific ansatz for that subdomain. In the same manner, the RHS represents the equivalent forces resulting from each subdomain. However, only two subdomains contribute as they are covered with a piezoelectric film.

6 Comparison between variational models

In this section, we compare the three variational models taking FEM simulations as a reference. We have also carried out a convergence analysis of these models over the displacement and the optical parameters ($F\#$ and RMSWFE).

6.1 Variational solutions versus FEM simulations

In the analyzed lenses, we use material parameters and structural dimensions for the membrane and the piezoelectric stack as specified in.[12] We have neglected the effect of platinum and adhesion layers of the piezoelectric stack on the membrane displacement. Moreover, we have only

considered actuation voltage ranges over which the resulting deformation is dominated by bending as opposed to stretching and the equation of the deflection is linear.

The variational solutions of the three models are obtained by solving the three linear systems of equations in Eqs. (24), (35) and (58) for the vector $\mathbf{C}$. Enhancing the accuracy of these solutions requires increasing the number of basis functions N. However, the higher the N value, the more prone these systems of equations are to become numerically ill-conditioned. That situation can be avoided by multiplying the equivalent stiffness matrix from left and right by diagonal matrices. This diagonal scaling minimizes the euclidean condition number;[22] defined as the ratio of the largest to the smallest singular value of the equivalent stiffness matrix. Thus, we propose a diagonal matrix whose elements are powers of the normalization factor of the Gegenbauer polynomials when their domain extends over the normalized interval $[-1, 1]$.[23] The normalization factor for any function $\phi_{lj}(X, Y)$ is

$$b_{lj} = \frac{[\Gamma(\beta)]^2}{\pi 2^{1-2\beta}} \left[\frac{l!j!(l+\beta)(j+\beta)}{\Gamma(l+2\beta)\Gamma(j+2\beta)} \right]^{1/2} \tag{59}$$

where $l, j = 0, 2, 4, \cdots$ are indices of the weighted Gegenbauer polynomials. $\beta = 9/2$ and $\Gamma(\cdot)$ is the Gamma function. For pupil opening ratios of interest, we have found that the fourth power is the minimum to dodge numerically ill-conditioning in these linear systems of equations.

Figure 5 shows displacement profiles from variational solutions and FEM simulations for various pupil opening ratios. Models 0 and 1 show similar behavior when pupil opening ratios are small and the Gegenbauer basis is used for most of the membrane area in model 1. Thus, for these ratios, the contribution of the Gegenbauer-basis terms to the electrical enthalpy of model 1 dominates other contributions and the curves resemble those of model 0 which uses this basis only. This

is evident for displacement profiles with $\gamma_1 < 0.6$, as shown in Fig. 5. The larger the value of γ_1 is, the more dissimilar are the displacement curves of the two models and the better is the agreement between model 1 and FEM.

Model 2 with $N = 3$ has the worst displacement approximation of all models for most pupil openings, but this improves with increasing N value. Model 2 with $N = 7$ provides better displacement approximations than the other models for all pupil openings of interest. In Fig. 5, this becomes particularly clear for the displacement curves of model 2 with $\gamma_1 \leq 0.3$ when compared to models 0 and 1.

To compare the variational solution for w_{N_G} of the different models to the FEM result w_{FEM}, we monitor the l_2 relative error norm given by

$$\zeta_w = \left[\frac{\sum (w_{FEM} - w_{N_G})^2}{\sum w_{FEM}^2} \right]^{1/2}. \tag{60}$$

The sums in the above equation are over a set of discrete points of the cross-sectional displacement profiles shown in Fig. 5. ζ_w curves for different models and various γ_1 values are shown in Fig. 6. It is evident that model 0 shows decreasing, in most cases, nonmonotonic trends for increasing N. However, model 1 shows smoothly decreasing trends and even reaches the highest accuracy at certain N values for γ_1 ratios ≥ 0.4 .

Model 2's approximations appear to be worse with lower order N, but they improve with increasing N. After $N = 7$, the error flatten for all pupil opening ratios of interest and model 2 reaches the highest accuracy. Thus, model 2 can outperform the other models with only 10 DOFs according to Tab. 1.

It is notable that the ζ_w curves do not converge to zero for any model. This is to be expected
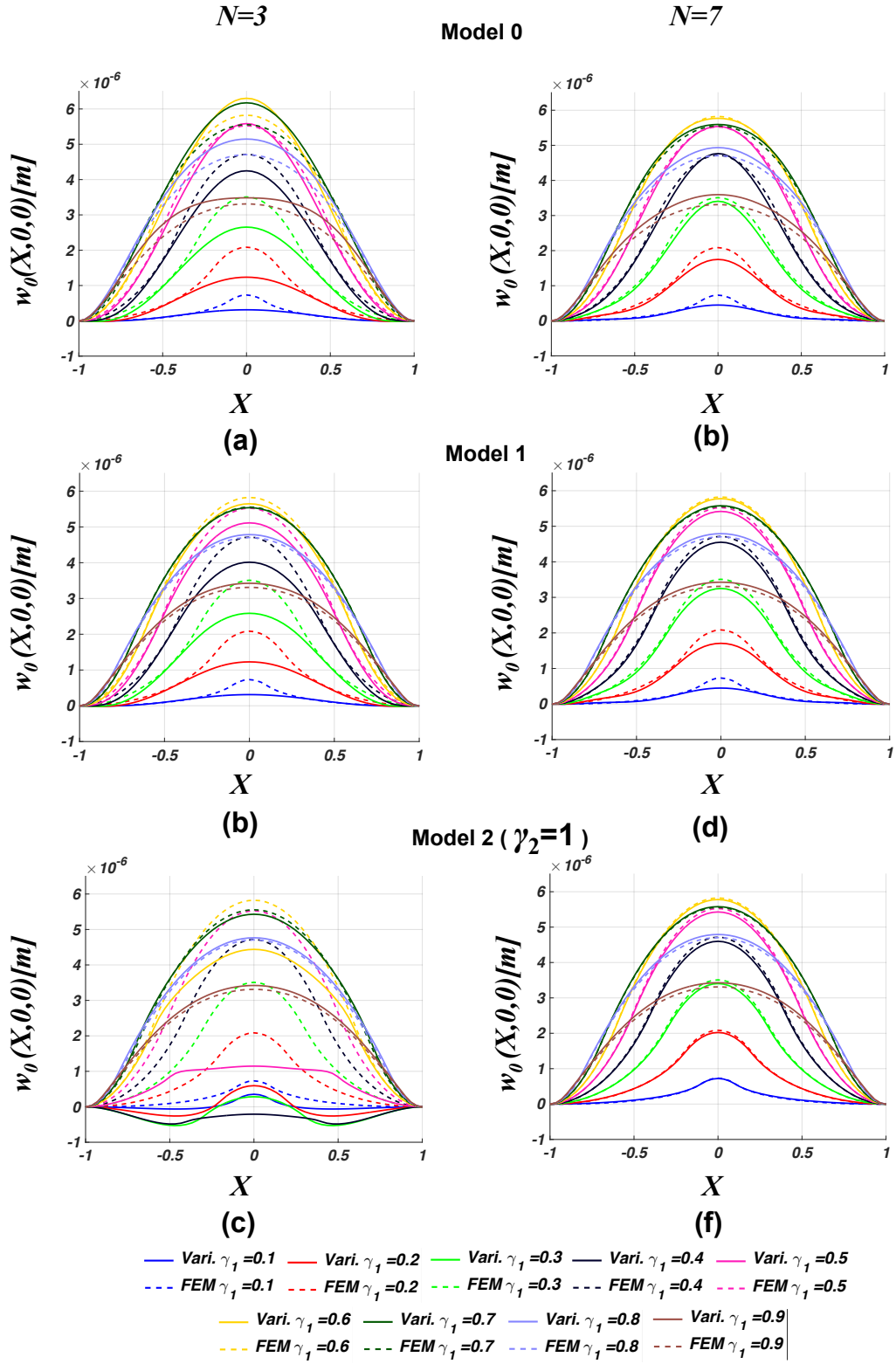
Fig 5 Displacement profiles in $xz-$plane from FEM and different models at $N = 3$ and $N = 7$ for different values of ratio γ_1 with piezoelectric material at $V_{\mathrm{p}} = -10V$.

because of the neglect of the inplane displacements. However, this elimination of DOFs that could have been assigned for inplane displacements has simplified the variational formulation significantly.
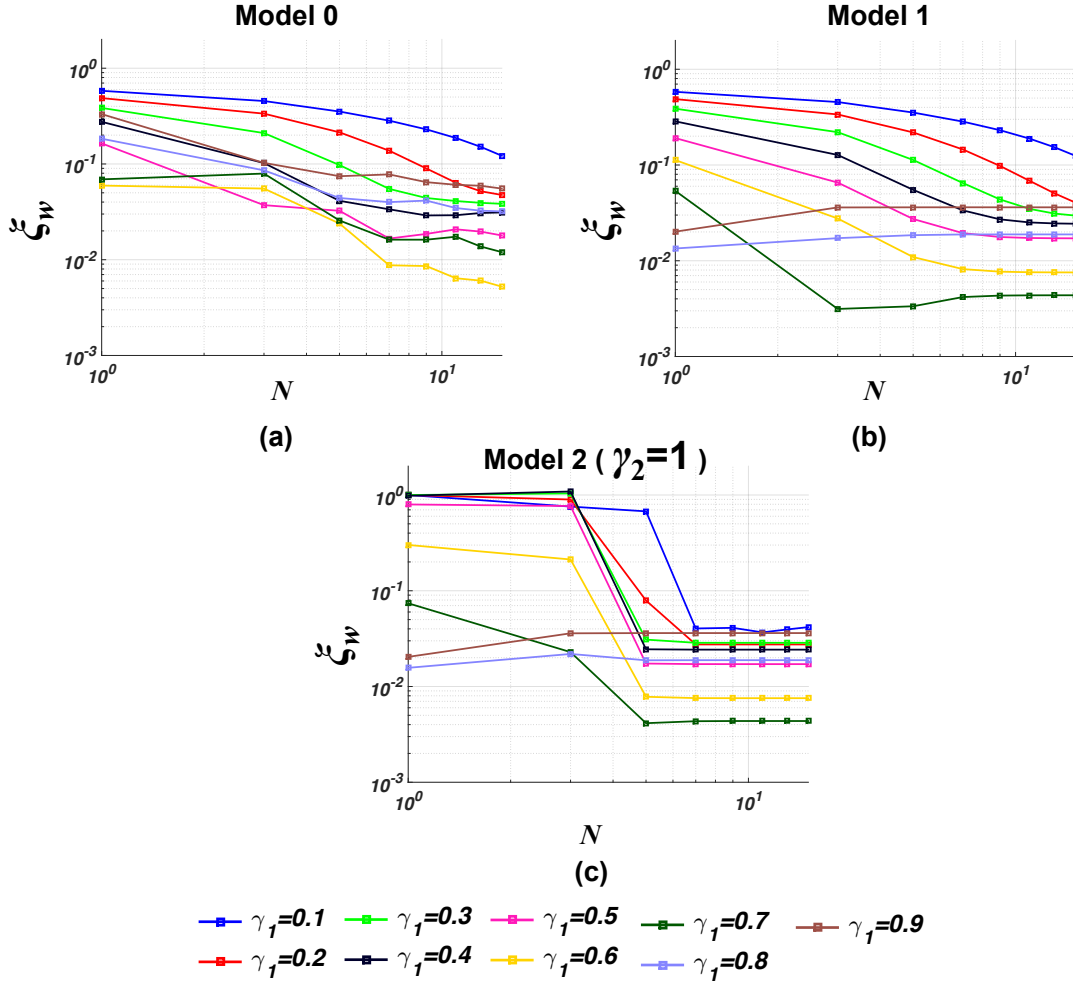

Fig 6 l_2 relative error norm for the displacement versus number of polynomials N for different models.

6.2 *Optical Simulations*

To evaluate the lens optical performance, we import the lens displacement from both variational solutions and FEM simulations on a 512×512 grid. We use ray tracing in an optical-design program (Zemax)[24] to evaluate the lens' optical parameters such as F-number ($F\#$) and RMSWFE. $F\#$ is defined as $f/(\gamma_1 a)$, where f is the focal length defined as the distance in between the lens'

flat surface to the minimum on-axis spot. The on-axis wavefront error (WFE) is the optical path difference between the constant phase surface of the wave coming out of the lens and a reference sphere having its center at the image plane and its radius equal to the seperating distance between lens exit pupil and the image plane.[24]

Figure 7 shows the optical parameters from different models with various N compared to those from FEM simulations. Model 0's approximations show oscillatory behavior for the optical parameters with increasing N similar to the ζ_w curves. Model 1's approximations approach the optical parameters from FEM in a more uniform way. For $\gamma_1 \leq 0.3$, approximations from models 0 and 1 become similar for the same reason mentioned earlier for their displacements.

For model 2 with $N = 1$, ζ_w is greater than 0.8 for most γ_1 values of interest. Thus, we have omitted optical parameters at that particular value of N. The optical parameters from Model 2 rapidly approach those of FEM and increasing the value of N above 7 does not add any further improvements.

To asses the ability of the variational models in approximating the optical parameters over various pupil openings, we monitor the l_2 relative error norms of $1/F\#$ and RMSWFE expressed as

$$\zeta_{1/F\#} = \left[\frac{\sum_{\gamma_1}(1/F\#_{\mathrm{FEM}} - 1/F\#_{\mathrm{Model}})^2}{\sum_{\gamma_1}(1/F\#_{\mathrm{FEM}})^2}\right]^{1/2}, \tag{61}$$
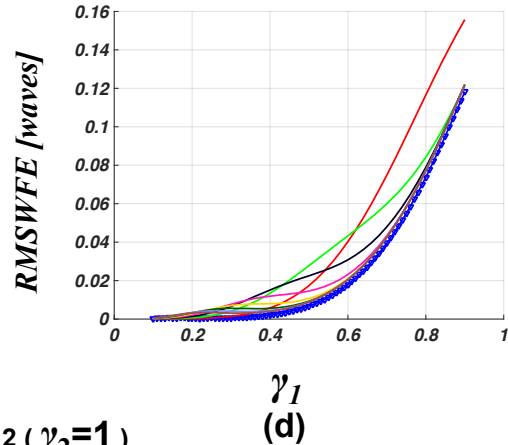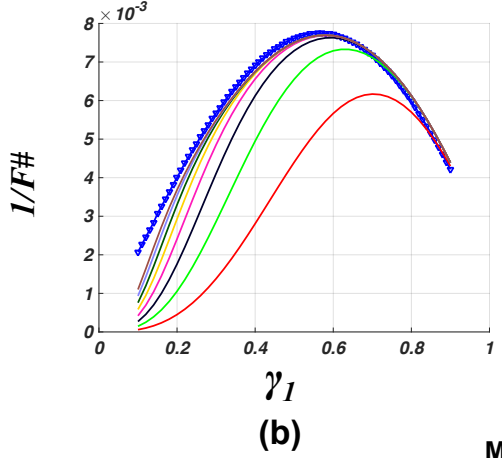
$$\zeta_{\mathrm{RMSWFE}} = \left[\frac{\sum_{\gamma_1}(\mathrm{RMSWFE}_{\mathrm{FEM}} - \mathrm{RMSWFE}_{\mathrm{Model}})^2}{\sum_{\gamma_1}(\mathrm{RMSWFE}_{\mathrm{FEM}})^2}\right]^{1/2}. \tag{62}$$

The sums in the above equations are over a set of lenses with γ_1 values ranging from 0.1 to 0.9 in steps of 0.02. In this aspect, the parameters $\zeta_{1/F\#}$ and ζ_{RMSWFE} will indicate the effectiveness of each variational model to approximate the lens' optical performance over a wide range of pupil
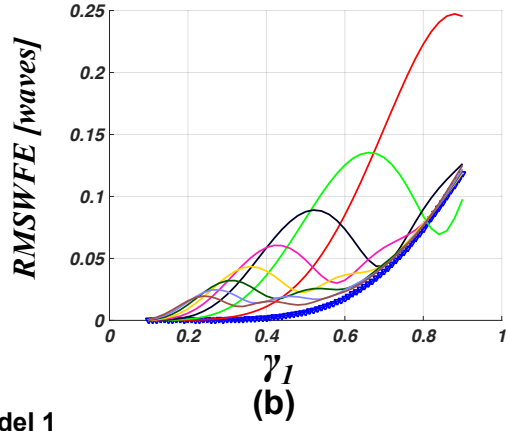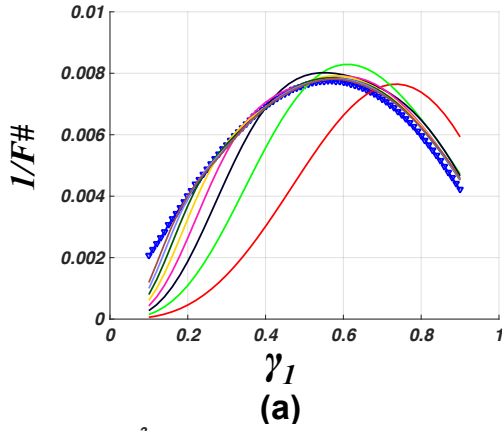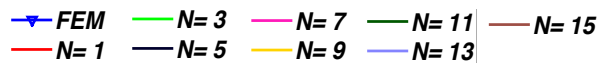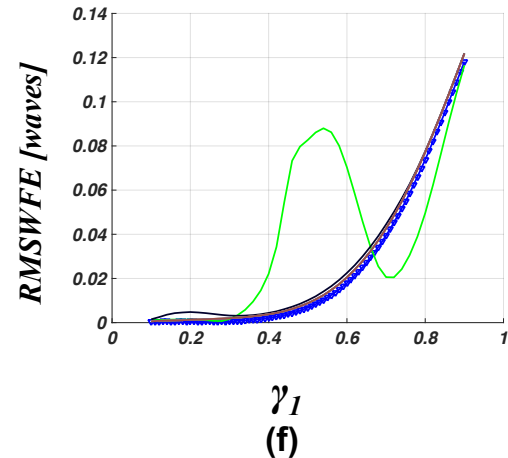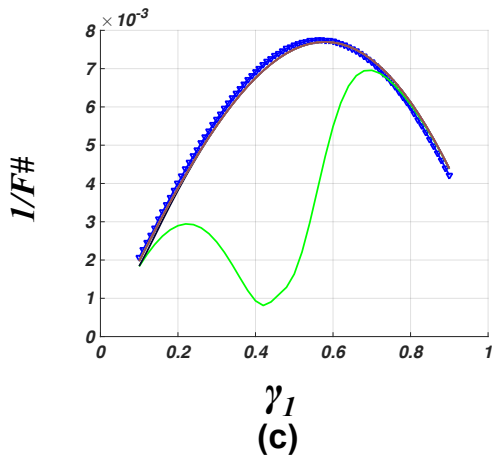
Fig 7 Reciprocal $F\#$ and RMSWFE versus the ratio γ_1, all with $V_\mathrm{p} = -10V$ and $\lambda = 550nm$ for the three models.

openings. Figure 8 shows these norms versus N for the three models. Model 0 and 1 show similar behaviors for $1/F\#$ curves, but model 1 shows an improved performance for RMSWFE curves. Model-1's ζ_{RMSWFE} curve is lower than the one for model 0 by nearly 50% at all N values. Model 2 starts on the wrong foot, but it becomes more accurate as N is increased. When N reaches 7, it becomes the most accurate among the other models. For $N \geq 7$, model 2 achieves accuracies of respectively 5.1% and 2.1% for RMSWFE and $1/F\#$.
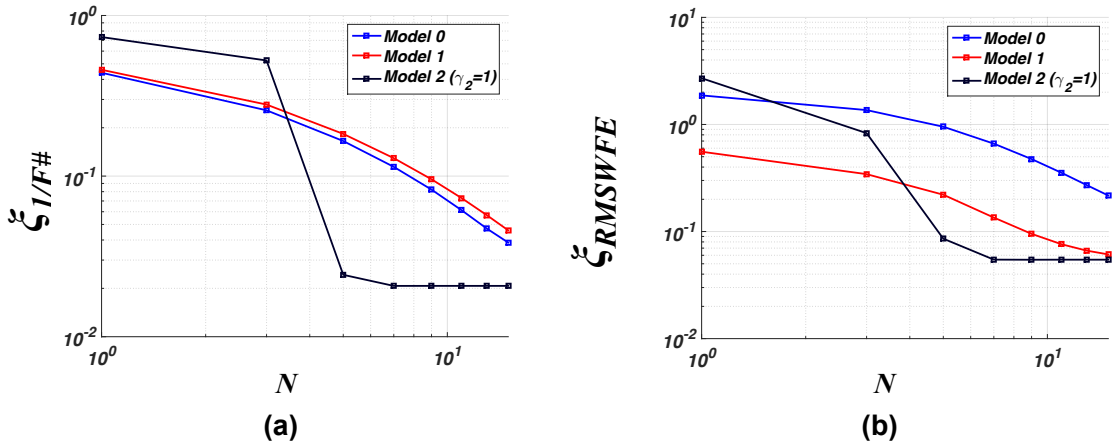

Fig 8 l_2 relative error norm of (a) reciprocal $F\#$ and (b) RMSWFE versus order N for three models.

7 Discussion

For a certain polynomial order, the three models have the same N_G DOFs but their accuracy varies depending on the type of basis functions. Model 2 has reduced these DOFs to only 10 as it uses the homogeneous solution of the plate differential equation over most of the membrane area. With the same DOFs, model 0 predicts RMSWFE and $1/F\#$ with the respective accuracies of 11.4% and 66.2%, as shown in Fig. 8. It has needed as much as 120 DOFs to bring the accuracies down to those of model 2 in order to provide an acceptable representation of the lens' optical performance.[12]

Models 1 and 2 represent an alternative route to low order models than generic methods such as the MOR methods mentioned in the introduction. Instead of using a a projection approach to

reduce a high-order problem, we have crafted problem-specific trial functions to yield accurate solution starting with a low-order ansatz.

Models 1 and 2 are powerful tools for optical wavefront representations because they can analytically yield the Zernike coefficients to represent the lens surface. Since the displacement ansatz inside the pupil region has the form of Fourier cosine series, it can be easily mapped to Zernike polynomials $Z_{n'}^{m'}$.[25] The squared value of Zernike coefficients is calculated through projection from

Model 1:

$$a_{n'm'}^2 = \int_0^1 \int_0^{2\pi} w_0^{(1)}(r) Z_{n'}^{m'}(r, \theta) r \mathrm{d}r \mathrm{d}\theta, \tag{63}$$

Model 2:

$$a_{n'm'}^2 = \int_0^1 \int_0^{2\pi} w_0^{(I)}(\alpha r) Z_{n'}^{m'}(r, \theta) r \mathrm{d}r \mathrm{d}\theta \tag{64}$$

where

$$Z_{n'}^{m'} = R_{n'}^{m'}(r) \cos(m'\theta)$$

$$= \sum_{k=0}^{\frac{n'-m'}{2}} \eta_{n'm'k} r^{n'-2k} \cos(m'\theta), \tag{65}$$

$$\eta_{n'm'k} = (-1)^k \binom{n'-k}{k} \binom{n'-2k}{\frac{n'-m'}{2}-k} \tag{66}$$

and n' and m' are nonnegative even integers due to the lens symmetry. Their respective maximum values are $N_F + 2$ and N_F from the $w_0^{(1)}$ (or $w_0^{(I)}$) expression and according to the definition of Zernike polynomials. In Eq. (64), the radial variable is scaled by the factor α since Zernike

polynomials are defined on a reference unit circle that is usually taken as the lens pupil.

From Eqs. (65) and (66), and substituting of $w_0^{(1)}$ into Eqs. (63) and (64), it equals

$$a_{n',m'}^2 = \zeta_{m'}\pi \sum_{k=0}^{\frac{n'-m'}{2}} \eta_{n'm'k}\left(\frac{A_{m'}^{\mathrm{I}}\tau_{A_{m'}}}{n'-2k+m'+2}\right.$$
$$\left.+ \frac{B_{m'}^{\mathrm{I}}\tau_{B_{m'}}}{n'-2k+m'+4}\right) \tag{67}$$

where A_i^{I} and B_i^{I} are the coefficients of the displacement ansatz' subfunction in the pupil area. $\zeta_{m'}$ is the Neumann factor that equals 2 if $m' = 0$ and 1 otherwise. Due to scaling of the radial variable, the correction factors τ are defined as

$$\textbf{Model 1:} \quad \tau_{A_0} = \tau_{B_0} = \tau_{A_{m'}} = \tau_{B_{m'}} = 1, \tag{68}$$

$$\textbf{Model 2:} \quad \tau_{A_0} = 1, \tau_{B_0} = \alpha^2, \tau_{A_{m'}} = \alpha^{m'},$$

$$\tau_{B_{m'}} = \alpha^{m'+2}. \tag{69}$$

In that manner, the reduced models can substitute the FEM mechanical simulations of the lens and directly provide the Zernike coefficients representing the lens sag. To be used in optimization, a MATLAB code with a Dynamic Data Exchange (DDE) extension can export the coefficients $a_{n',m'}$ to optical programs such as Zemax to directly represent the lens sag[24] and calculate the required optical performance metrics.

The reduced linear models are necessary foundations for building few-DOFs nonlinear models. Such models will include residual stresses[26,27] and geometric nonlinearities[28] due to biasing, and involve solving a system of cubic equations of motion.[28,29] This system of equations is difficult to be solved semi-analytically with many DOFs because of the tremendous number of integrals to be

37

calculated for the quadratic and cubic stiffnesses.

8 Conclusions

We have introduced two reduced-order variational models to predict the linear optoelectromechanical performance of piezoelectrically actuated MEMS tunable lenses. The reduction in model order is due to using a piecewise expansion of trial functions that have different forms in the lens' pupil and the actuator areas. In particular, we used the exact solution for the elastic plate differential equation in the central lens area. The larger this area is, the lower is the number of DOFs needed to reach high accuracy in terms of mechanical and optical parameters. For example, model 2 needs only 10 DOFs to achieve accuracies of respectively 5.1% and 2.1% for RMSWFE and $1/F\#$.

The ansatz subfunction in the pupil region of the presented models can be easily mapped to Zernike polynomials to represent the lens surface. The Zernike coefficients are obtained on closed form in terms of model DOFs. This enables fast computations of lens optical performance which is useful when optimizing lens designs by extensive exploration of dimensions and material parameters.

References

1 Y. Tseng, "Voice coil motor apparatus," (2008). US Patent 7,400,068.

2 C. Zhao, *Ultrasonic motors: Technologies and applications*, Science Press Beijing and Springer-Verlag Berlin Heidelberg (2011).

3 K. Haugholt, D. Wang, F. Tyholdt, *et al.*, "Polymer lens," (2012). US Patent 8,199,410.

4 M. Ye, B. Wang, and S. Sato, "Liquid-crystal lens with a focal length that is variable in a wide range," *Appl. Opt.* **43**, 6407–6412 (2004). [doi:10.1364/AO.43.006407].

5 N. Chronis, G. Liu, K.-H. Jeong, *et al.*, "Tunable liquid-filled microlens array integrated with microfluidic network," *Opt. Express* **11**, 2370–2378 (2003). [doi:10.1364/OE.11.002370].

6 A. Werber and H. Zappe, "Tunable microfluidic microlenses," *Appl. Opt.* **44**, 3238–3245 (2005). [doi:10.1364/AO.44.003238].

7 S. Kuiper, B. H. Hendriks, L. J. Huijbregts, *et al.*, "Variable-focus liquid lens for portable applications," *Proc. SPIE* **5523**, 100–109 (2004). [doi:10.1117/12.555980].

8 U. Wallrabe, "Axicons et al. - highly aspherical adaptive optical elements for the life sciences," in *2015 18th International Conference on Solid-State Sensors, Actuators and Microsystems (TRANSDUCERS), 2015 Transducers*, 251–256 (2015). [doi:10.1109/TRANSDUCERS.2015.7180909].

9 T. Bechtold, G. Schrag, and L. Feng, Eds., *System-level modeling of MEMS*, Wiley-VCH Verlag GmbH & Co. KGaA (2013).

10 R. Hegarty and T. Ariman, "Elasto-dynamic analysis of rectangular plates with circular holes," *International Journal of Solids and Structures* **11**(7), 895 – 906 (1975). [doi:10.1016/0020-7683(75)90012-8].

11 K. Torabi and A. Azadi, "A new approach to the study of transverse vibrations of a rectangular plate having a circular central hole," *Journal of Solid Mechanics* **6**(2), 135–149 (2014).

12 M. A. Farghaly, M. N. Akram, and E. Halvorsen, "Modeling framework for piezo-

electrically actuated mems tunable lenses," *Opt. Express* **24**, 28889–28904 (2016). [doi:10.1364/OE.24.028889].

13 M. K. Kwak and S. Han, "Free vibration analysis of rectangular plate with a hole by means of independent coordinate coupling method," *Journal of Sound and Vibration* **306**(1), 12 – 30 (2007). [doi:10.1016/j.jsv.2007.05.041].

14 L. G. M. Olson Mervyn D. and H. A. Tulloch, "Finite plate-bending elements in polar co-ordinates." NATIONAL AERONAUTICAL ESTABLISHMENT OTTAWA (ONTARIO) (1968).

15 G. C. Pardoen, "Asymmetric bending of circular plates using the finite element method," *Computers & Structures* **5**(2), 197 – 202 (1975). [doi:10.1016/0045-7949(75)90010-3].

16 J. N. Reddy, *Mechanics of laminated composite plates and shells: Theory and analysis*, CRC press, 2nd ed. (2004).

17 H. F. Tiersten, "Hamilton's principle for linear piezoelectric media," *Proceedings of the IEEE* **55**, 1523–1524 (1967). [doi:10.1109/PROC.1967.5887].

18 J. N. Reddy, *Applied functional analysis and variational methods in Engineering*, McGraw-Hil (1986).

19 M. A. Farghaly, M. N. Akram, and E. Halvorsen, "Optical performance of piezoelectrically actuated mems tunable lenses with various pupil geometries," *Optical Engineering* **56**(3), 035104 (2017). [doi:10.1117/1.OE.56.3.035104].

20 *MathWorks*. https://www.mathworks.com/products/matlab.html.

21 M. H. Jawad, *Theory and Design of Plate and Shell Structures*, Springer US (1994).

22 R. D. Braatz and M. Morari, "Minimizing the euclidean condition number," *SIAM Journal on Control and Optimization* **32**(6), 1763–1768 (1994). [doi:10.1137/S0363012992238680].

23 F. W. J. Olver, D. W. Lozier, R. F. Boisvert, *et al.*, *NIST handbook of mathematical functions*, Cambridge Univeristy press, New York (2010).

24 Zemax LLC, Washington, USA, *Zemax 13 Optical Design program* (2015).

25 V. N. Mahajan, "Zernike circle polynomials and optical aberrations of systems with circular pupils," *Appl. Opt.* **33**, 8121–8124 (1994). [doi:10.1364/AO.33.008121].

26 E. Hong, R. Smith, S. Krishnaswamy, *et al.*, "Residual stress development in pb(zr,ti)o3/zro2/sio2 stacks for piezoelectric microactuators," *Thin Solid Films* **510**(1), 213 – 221 (2006).

27 S. Corkovic, R. W. Whatmore, and Q. Zhang, "Development of residual stress in sol-gel derived pb(zr,ti)o3 films: An experimental study," *Journal of Applied Physics* **103**(8), 084101 (2008).

28 G. Singh, G. V. Rao, and N. Iyengar, "Some observations on the large deflection bending of rectangular antisymmetric cross-ply plates," *Composite Structures* **18**(1), 77 – 91 (1991).

29 S. D. Senturia, *Microsystem Design*, Kluwer Academic Press (2001).

Appendix A: Variational energy integrals for model 0

The elements in the matrices $\mathbf{R}_{k_1 k_2}^{\Omega_q}$ ($q = 1, 2$) and $\mathbf{F}_{k_2}$ are

$$R_{k_1 k_2}^{\Omega_q} = \frac{1}{(a/2)^2} \int_{\Omega_q} \left\{ D_{11,\Omega_q}^* \Phi_{k_1,XX} \Phi_{k_2,XX} \right.$$

$$+ D_{12,\Omega_q}^* \Phi_{k_1,YY} \Phi_{k_2,XX}$$

$$+ D_{12,\Omega_q}^* \Phi_{k_1,XX} \Phi_{k_2,YY}$$

$$+ D_{22,\Omega_q}^* \Phi_{k_1,YY} \Phi_{k_2,YY}$$

$$\left. + 4 D_{66,\Omega_q}^* \Phi_{k_1,XY} \Phi_{k_2,XY} \right\} \mathrm{d}X \mathrm{d}Y, \tag{70}$$

$$F_{k_2} = -V_\mathrm{p} \bar{z}_\mathrm{p} \bar{e}_{31} \int_0^1 \int_0^{2\pi} \nabla^2 \widetilde{\Phi}_{k_2} r \mathrm{d}r \mathrm{d}\theta. \tag{71}$$

A simple way to numerically calculate the above matrix elements is through using a series expansion of Gegenbauer polynomials and integration masks described in details in Refs. 12, 19.

Appendix B: Model 1

The analytic expression of the inverse of sub-matrices inverses $\mathbf{L}_{i,\mathrm{I}}$ can be expressed as

$$\mathbf{L}_{i,\mathrm{I}}^{-1} = \begin{bmatrix} (i+2)r^{-i}/2 & -r^{1-i}/2 \\ -ir^{-i-2}/2 & r^{-1-i}/2 \end{bmatrix}. \tag{72}$$

The matrices $\mathbf{N}_{1,\mathrm{I}}$ and $\mathbf{T}_{1,1}$ using the first basis function Φ_1 are given by

$$\mathbf{N}_{1,\mathrm{I}} = \begin{bmatrix} 3\gamma_1^8/128 - \gamma_1^6/4 + 5\gamma_1^4/4 - 2\gamma_1^2 + 1 \\ \gamma_1^2(3\gamma_1^6 - 24\gamma_1^4 + 80\gamma_1^2 - 64)/16 \\ 0 \\ 0 \\ -\gamma_1^4(\gamma_1^4 - 8\gamma_1^2 + 8)/32 \\ -\gamma_1^4(\gamma_1^4 - 6\gamma_1^2 + 4)/4 \\ 0 \\ 0 \\ \gamma_1^8/128 \\ \gamma_1^8/16 \end{bmatrix}, \tag{73}$$

$$\mathbf{T}_{1,1} = \begin{bmatrix} t_{1,1} & t_{2,1} & \cdots & t_{10,1} \end{bmatrix}^T \tag{74}$$

where

$$t_{1,1} = \frac{5}{4}\gamma_1^4 - 2\gamma_1^2 - \frac{1}{32}\gamma_1^2(3\gamma_1^6 - 24\gamma_1^4 + 80\gamma_1^2 - 64)$$

$$- \frac{1}{4}\gamma_1^6 + \frac{3}{128}\gamma_1^8 + 1,$$

$$t_{2,1} = \frac{1}{32}\gamma_1^2(3\gamma_1^6 - 24\gamma_1^4 + 80\gamma_1^2 - 64),$$

$$t_{5,1} = \frac{1}{8}\gamma_1^4(\gamma_1^4 - 6\gamma_1^2 + 4) - \frac{3}{32}\gamma_1^4(\gamma_1^4 - 8\gamma_1^2 + 8),$$

$$t_{6,1} = \frac{1}{16}\gamma_1^4(\gamma_1^4 - 8\gamma_1^2 + 8) - \frac{1}{8}\gamma_1^4(\gamma_1^4 - 6\gamma_1^2 + 4),$$

$$t_{8,1} = \frac{1}{128}\gamma_1^8,$$

$$t_{3,1} = t_{4,1} = t_{7,1} = t_{8,1} = t_{10,1} = 0.$$

Appendix C: Variational energy integrals for models 1 and 2

The spring and force variational terms over circular and ring subdomains are given as

$$R_\circ(w_0, \delta w_0; \mathbf{D}_{\Omega_q}^*, \gamma_0, \alpha_H, \alpha_L) = \delta \mathbf{A}^T \mathbf{H}^{\Omega_q} \mathbf{A}, \tag{75}$$

$$F_\circ(\delta w_0; \alpha_H, \alpha_L) = V_p \bar{z}_p \bar{e}_{31} \delta \mathbf{A}^T \mathbf{F} \tag{76}$$

where

$$\mathbf{H}^{\Omega_q} = \frac{1}{\gamma_0^2(a/2)^2} \Big(D_{11,\Omega_q}^* \mathbf{H}^{I_1} + D_{12,\Omega_q}^* \left(\mathbf{H}^{I_2} + \mathbf{H}^{I_3} \right)$$

$$+ D_{22,\Omega_q}^* \mathbf{H}^{I_4} + 4D_{66,\Omega_q}^* \mathbf{H}^{I_5} \Big), \tag{77}$$

$$
\mathbf{H}^{\mathrm{I}_m} = \begin{bmatrix} \mathbf{H}_0^{\mathrm{I}_m} & \mathbf{0} & \mathbf{0} & \cdots & \mathbf{0} \\ \mathbf{0} & \mathbf{H}_2^{\mathrm{I}_m} & \mathbf{0} & \cdots & \mathbf{0} \\ \vdots & & \ddots & & \mathbf{0} \\ \mathbf{0} & \mathbf{0} & \mathbf{0} & \cdots & \mathbf{H}_{N_F}^{\mathrm{I}_m} \end{bmatrix},
$$

$$
\mathbf{A} = \begin{bmatrix} \mathbf{A}_0 \\ \mathbf{A}_2 \\ \vdots \\ \mathbf{A}_{N_F} \end{bmatrix}, \quad \mathbf{A}_i = \begin{bmatrix} A_i \\ B_i \\ C_i \\ D_i \end{bmatrix}, \tag{78}
$$

$$
\mathbf{F} = \begin{bmatrix} \mathbf{F}_0 \\ \mathbf{F}_2 \\ \vdots \\ \mathbf{F}_{N_F} \end{bmatrix}. \tag{79}
$$

The submatrix $\mathbf{0}$ is 4×4 zero matrix. In Eq. (75), each term $\mathbf{H}^{\mathrm{I}_m}$ where $m = 1, 2, \cdots 5$ represents one of the five integral terms of Eq. (4). The matrices $\mathbf{H}^{\mathrm{I}_2}$ and $\mathbf{H}^{\mathrm{I}_3}$ are equal. Expressions for the submatrices $\mathbf{H}_i^{\mathrm{I}_m}$ are listed below. To simplify introducing these submatrices, we define two vector-valued functions

$$
\vec{\Psi}_0 = \begin{bmatrix} 1 \\ r^2 \\ \ln(r) \\ r^2 \ln(r) \end{bmatrix}, \quad \vec{\Psi}_n = \begin{bmatrix} r^n \\ r^{n+2} \\ r^{-n} \\ r^{-n+2} \end{bmatrix} \cos(n\theta). \tag{80}
$$

45

$\mathbf{H}^{I_1} = \int_0^r \int_0^{2\pi} \vec{\Psi}_{n,rr} \vec{\Psi}_{n,rr}^T \, r\,dr\,d\theta$:

$$\mathbf{H}^{I_1}_0 = \begin{bmatrix}
0 & 0 & 0 & 0 \\
0 & 4\pi r^2 & -4\pi\ln(r) & 4\pi r^2(\ln(r)+1) \\
0 & -4\pi\ln(r) & -\pi r^{-2} & -2\pi\ln(r)(\ln(r)+3) \\
0 & 4\pi r^2(\ln(r)+1) & -2\pi\ln(r)(\ln(r)+3) & \pi r^2(8\ln(r)+4(\ln(r))^2+5)
\end{bmatrix} ,$$

$$\mathbf{H}^{I_1}_n = \begin{bmatrix}
\frac{\pi}{2}(n-1)n^2 r^{2n-2} & -\frac{\pi}{4}r^{2n}(-2n^3-4n^2+2n+4) & -\frac{\pi}{2r^2}n^2(n^2-1) & \pi n\ln(r)(n-1)^2(n-2) \\
-\frac{\pi}{4}r^{2n}(-2n^3-4n^2+2n+4) & \frac{\pi}{2}r^{2n+2}(n+1)^2(n+2)^2 & \pi n\ln(r)(n+1)^2(n+2) & \frac{\pi}{2}r^2(n^4-5n^2+4) \\
-\frac{\pi}{2r^2}n^2(n^2-1) & \pi n\ln(r)(n+1)^2(n+2) & -\pi n^2(n+1)/(2r^{2n+2}) & \pi(-n^3+2n^2+n-2)/(2r^{2n}) \\
\pi n\ln(r)(n-1)^2(n-2) & \frac{\pi}{2}r^2(n^4-5n^2+4) & \pi(-n^3+2n^2+n-2)/(2r^{2n}) & -\frac{\pi}{2}r^{2-2n}(n-1)(n-2)^2
\end{bmatrix} ,$$

$\mathbf{H}^{I_2} = \int_0^r \int_0^{2\pi} \left(\frac{1}{r}\vec{\Psi}_{n,r} + \frac{1}{r^2}\vec{\Psi}_{n,\theta\theta}\right)\vec{\Psi}_{n,rr}^T \, r\,dr\,d\theta$:

$$\mathbf{H}^{I_2}_0 = \begin{bmatrix}
0 & 0 & 0 & 0 \\
0 & 4\pi r^2 & 0 & 2\pi r^2(2\ln(r)+1) \\
0 & 0 & \pi r^{-2} & 2\pi\ln(r) \\
0 & 2\pi r^2(2\ln(r)+1) & 2\pi\ln(r) & \pi r^2(8\ln(r)+4(\ln(r))^2+5)
\end{bmatrix} ,$$

$$\mathbf{H}^{I_2}_n = \begin{bmatrix}
-\frac{\pi}{2}n^2 r^{2n-2}(n-1) & \frac{\pi}{2}r^{2n}(-n^3+n) & -\pi(-n^4+n^2)/(2r^2) & -\pi n^2\ln(r)(n-1)^2 \\
\frac{\pi}{2}r^{2n}(-n^3+n) & \pi r^{2n+2}(-n^3/2-n^2/2+2n+2) & -\pi n^2\ln(r)(n+1)^2 & -\frac{\pi}{2}r^2(n^4+3n^2-4) \\
-\pi(-n^4+n^2)/(2r^2) & -\pi n^2\ln(r)(n+1)^2 & \pi n^2(n+1)/(2r^{2n+2}) & -\pi(-n^3+n)/(2r^{2n}) \\
-\pi n^2\ln(r)(n-1)^2 & -\frac{\pi}{2}r^2(n^4+3n^2-4) & -\pi(-n^3+n)/(2r^{2n}) & -\pi r^{2-2n}(-n^3/2+n^2/2+2n-2)
\end{bmatrix} ,$$

$$\mathbf{H}^{I_4}=\int_0^r\int_0^{2\pi}\left(\tfrac{1}{r}\vec{\Psi}_{n,r}+\tfrac{1}{r^2}\vec{\Psi}_{n,\theta\theta}\right)\left(\tfrac{1}{r}\vec{\Psi}_{n,r}^T+\tfrac{1}{r^2}\vec{\Psi}_{n,\theta\theta}^T\right)r\,dr\,d\theta:$$

$$\mathbf{H}_0^{I_4}=\begin{bmatrix}
0 & 0 & 0 & 0 \\
0 & 4\pi r^2 & 4\pi\ln(r) & 4\pi r^2(\ln(r)+1) \\
0 & 4\pi\ln(r) & -\pi r^{-2} & 2\pi\ln(r)(\ln(r)+1) \\
0 & 4\pi r^2(\ln(r)+1) & 2\pi\ln(r)(\ln(r)+1) & \pi r^2(4(\ln(r))^2+1)
\end{bmatrix},$$

$$\mathbf{H}_n^{I_4}=\begin{bmatrix}
\frac{\pi}{2}n^2 r^{2n-2}(n-1) & -\frac{\pi}{4}r^{2n}(-2n^3+4n^2+2n-4) & -\frac{\pi}{2}n^2(n^2-1)/r^2 & \pi n\ln(r)(n-1)^2(n+2) \\
-\frac{\pi}{4}r^{2n}(-2n^3+4n^2+2n-4) & \frac{\pi}{2}r^{2n+2}(n+1)(n-2)^2 & \pi n\ln(r)(n+1)^2(n-2) & \frac{\pi}{2}r^2(n^4-5n^2+4) \\
-\frac{\pi}{2}n^2(n^2-1)/r^2 & \pi n\ln(r)(n+1)^2(n-2) & -\pi n^2(n+1)/(2r^{2n+2}) & \pi(-n^3-2n^2+n+2)/(2r^{2n}) \\
\pi n\ln(r)(n-1)^2(n+2) & \frac{\pi}{2}r^2(n^4-5n^2+4) & \pi(-n^3-2n^2+n+2)/(2r^{2n}) & -\frac{\pi}{2}r^{2-2n}(n-1)(n+2)^2
\end{bmatrix},$$

$$\mathbf{H}^{I_5}=4\int_0^r\int_0^{2\pi}\left(\tfrac{1}{r}\vec{\Psi}_{n,r\theta}-\tfrac{1}{r^2}\vec{\Psi}_{n,\theta}\right)\left(\tfrac{1}{r}\vec{\Psi}_{n,r\theta}^T-\tfrac{1}{r^2}\vec{\Psi}_{n,\theta}^T\right)r\,dr\,d\theta:$$

$$\mathbf{H}_0^{I_5}=\begin{bmatrix}
0 & 0 & 0 & 0 \\
0 & 0 & 0 & 0 \\
0 & 0 & 0 & 0 \\
0 & 0 & 0 & 0
\end{bmatrix},$$

$$\mathbf{H}_n^{I_5}=\begin{bmatrix}
2\pi n^2 r^{2n-2}(n-1) & 2\pi n r^{2n}(n^2-1) & 2\pi n^2(n^2-1)/r^2 & -4\pi n^2\ln(r)(n-1)^2 \\
2\pi n r^{2n}(n^2-1) & 2\pi n^2 r^{2n+2}(n+1) & -4\pi n^2\ln(r)(n+1)^2 & -2\pi n^2 r^2(n^2-1) \\
2\pi n^2(n^2-1)/r^2 & -4\pi n^2\ln(r)(n+1)^2 & -2\pi n^2(n+1)/r^{2n+2} & -2\pi n(n^2-1)/r^{2n} \\
-4\pi n^2\ln(r)(n-1)^2 & -2\pi n^2 r^2(n^2-1) & -2\pi n(n^2-1)/r^{2n} & -2\pi n^2 r^{2-2n}(n-1)
\end{bmatrix}.$$

The dashed lines are to ease visualizing the upper left quadrant of the matrices $\mathbf{H}_n^{I_i}$ which is used in models 1 and 2. The matrix $\mathbf{F}$ and its submatrics are given by

$$\mathbf{F} = \int_0^r \int_0^{2\pi} \left(\vec{\Psi}_{n,rr} + \frac{1}{r}\vec{\Psi}_{n,r} + \frac{1}{r^2}\vec{\Psi}_{n,\theta\theta} \right) r \mathrm{d}r \mathrm{d}\theta$$

$$\mathbf{F}_0 = \begin{bmatrix} 0 \\ 4\pi r^2 \\ 0 \\ 2\pi r^2(1 + 2\ln(r)) \end{bmatrix},$$

$$\mathbf{F}_n = \begin{bmatrix} 0 \\ 0 \\ 0 \\ 0 \end{bmatrix}.$$

Appendix D: Moment and shear force continuity conditions

Here we investigate the continuity conditions for the radial moments and shear forces assuming that the continuity conditions over displacement and slope are satisfied. Since there is no difference in layer structures in model 2 at the fictitious boundary, there is no change in the flexural stiffnesses D_{ij}^*. The radial moment and vertical shear force are given by[16]

$$M_{rr} = -D_{11}^* w_{0,rr} + \frac{D_{12}^*}{r}\left(w_{0,r} + w_{0,\theta\theta}\right), \tag{81}$$

$$\begin{aligned} Q_r = &-D_{11}^*(\frac{w_{0,rr}}{r} + w_{0,rrr}) \\ &- (D_{12}^* + 2D_{66}^*)\frac{w_{0,\theta\theta r}}{r^2} \\ &+ (D_{12}^* + 2D_{66}^* + D_{22}^*)\frac{w_{0,\theta\theta}}{r^3} + D_{22}^*\frac{w_{0,r}}{r^2}. \end{aligned} \tag{82}$$

Using Eq. (16), $w_{0,\theta\theta}$ becomes

$$w_{0,\theta\theta} = -\sum_{n=2,\cdots even}^{N_{s,k}} n^2 f_{k,n}(r,\gamma_0)\cos(n\theta). \tag{83}$$

Due to the orthogonality property of the trigonometric functions, the Fourier coefficients (for $n \geq$ 2) of $w_{0,\theta\theta}$ are related to those of w_0 by

$$f_{k,n}^{w_{0,\theta\theta}} = -n^2 f_{k,n}^{w_0}. \tag{84}$$

Thus, at the fictitious bonudary $w_{0,\theta\theta}$ is continuous as long as w_0 is continuous. From Eq. (81), the only term left to satisfy moment continuity is to enforce a continuity condition on the second derivative of the displacement. In a similar manner, the continuity of the third derivative of the displacement corresponds to the continuity for vertical radial shear force Q_r.

Appendix E: Model 2

The analytic expression of the inverse of the submatrices $\mathbf{L}_{0,\mathrm{II}}$ and $\mathbf{L}_{n,\mathrm{II}}$ can be expressed as

$$
\mathbf{L}_{0,\mathrm{II}}^{-1} =
\left[
\begin{array}{cc|cc}
1 & -r(\ln(r)+2)/4 & r^2\ln(r)/4 & -r^3(\ln(r)-1)/4 \\[4pt]
0 & (\ln(r)+2)/(4r) & -\ln(r)/4 & -r(\ln(r)+1)/4 \\[2pt]
\hline
0 & r/4 & -r^2/4 & r^3/4 \\[4pt]
0 & -1/(4r) & 1/4 & r/4
\end{array}
\right],
\tag{85}
$$

$$
\mathbf{L}_{n,\mathrm{II}}^{-1} =
\left[
\begin{array}{cc|cc}
\frac{(n^2-4)r^{-n}}{8(n-1)} & \frac{(n^2+3n-1)r^{1-n}}{8n(n-1)} & \frac{-r^{2-n}}{8n} & \frac{-r^{3-n}}{8n(n-1)} \\[6pt]
\frac{-n(n-2)r^{-n-2}}{8(n+1)} & \frac{-(n^2-n+1)r^{-n-1}}{8n(n+1)} & \frac{r^{-n}}{8n} & \frac{r^{1-n}}{8n(n+1)} \\[4pt]
\hline
\frac{-r^n(n^2-4)}{8(n+1)} & \frac{-r^{n+1}(-n^2+3n+1)}{8n(n+1)} & \frac{r^{n+2}}{8n} & \frac{-r^{n+3}}{8n(n+1)} \\[6pt]
\frac{n(n+2)r^{n-2}}{8(n-1)} & \frac{-r^{n-1}(n^2+n+1)}{8n(n-1)} & \frac{-r^n}{8n} & \frac{r^{n+1}}{8n(n-1)}
\end{array}
\right].
\tag{86}
$$

The matrices $\mathbf{N}_{1,\mathrm{II}}$, $\mathbf{T}_{1,\mathrm{II}}$ and $\mathbf{T}_{1,\mathrm{I}}$ using the first base function Φ_1, are given by

$$
\mathbf{N}_{1,\mathrm{II}} =
\begin{bmatrix}
3\gamma_0^8/128 - \gamma_0^6/4 + 5\gamma_0^4/4 - 2\gamma_0^2 + 1 \\
\gamma_0^2(3\gamma_0^6 - 24\gamma_0^4 + 80\gamma_0^2 - 64)/16 \\
\gamma_0^2(21\gamma_0^6 - 120\gamma_0^4 + 240\gamma_0^2 - 64)/16 \\
3\gamma_0^4(21\gamma_0^4 - 80\gamma_0^2 + 80)/8 \\
0 \\
0 \\
0 \\
0 \\
-\gamma_0^4(\gamma_0^4 - 8\gamma_0^2 + 8)/32 \\
-\gamma_0^4(\gamma_0^4 - 6\gamma_0^2 + 4)/4 \\
-\gamma_0^4(7\gamma_0^4 - 30\gamma_0^2 + 12)/4 \\
-3\gamma_0^4(7\gamma_0^4 - 20\gamma_0^2 + 4)/2 \\
0 \\
0 \\
0 \\
0 \\
\gamma_0^8/128 \\
\gamma_0^8/16 \\
7\gamma_0^8/16 \\
21\gamma_0^8/8
\end{bmatrix}
, \tag{87}
$$

51

$$\mathbf{T}_{1,\mathrm{II}} = \begin{bmatrix} 243\gamma_2^8/128 - 7\gamma_2^6 + 25\gamma_2^4/4 + 1 \\[1mm] -\gamma_2^2(15\gamma_2^6 - 54\gamma_2^4 + 40\gamma_2^2 + 16)/8 \\[1mm] \gamma_2^4(27\gamma_2^4 - 96\gamma_2^2 + 80)/16 \\[1mm] \gamma_2^4(9\gamma_2^4 - 36\gamma_2^2 + 40)/4 \\[1mm] 0 \\[1mm] 0 \\[1mm] 0 \\[1mm] 0 \\[1mm] \gamma_2^4(5\gamma_2^4 - 16)/64 \\[1mm] -\gamma_2^6(3\gamma_2^2 - 8)/32 \\[1mm] \gamma_2^8/64 \\[1mm] -\gamma_2^8/32 \\[1mm] 0 \\[1mm] 0 \\[1mm] 0 \\[1mm] 0 \\[1mm] \gamma_2^8/128 \\[1mm] 0 \\[1mm] 0 \\[1mm] 0 \end{bmatrix}, \tag{88}$$

$$\mathbf{T}_{1,\mathrm{I}} = \begin{bmatrix} t_{1,1} & t_{2,1} & \cdots & t_{10,1} \end{bmatrix}^T \tag{89}$$

where

$$t_{1,1} = \frac{15}{4}\gamma_2^4 - 4\gamma_2^6 + \frac{135}{128}\gamma_2^8$$
$$+ \alpha^2\left(-5\gamma_2^4 + \frac{9}{2}\gamma_2^6 - \frac{9}{8}\gamma_2^8\right)$$
$$+ \ln\alpha\left(5\gamma_2^4 - 6\gamma_2^6 + \frac{27}{16}\gamma_2^8\right) + 1,$$

$$t_{2,1} = \frac{\gamma_2^2}{32\alpha^2}\Big(80\gamma_2^2 - 96\gamma_2^4 + 27\gamma_2^6$$
$$+ \alpha^2\left(-64 + 72\gamma_2^4 - 24\gamma_2^6\right)$$
$$+ \alpha^2 \ln\alpha\left(320\gamma_2^2 - 288\gamma_2^4 + 72\gamma_2^6\right)\Big),$$

$$t_{5,1} = \frac{\gamma_2^4}{64\alpha^8}\left(5\gamma_2^4\alpha^8 - 8\gamma_2^4\alpha^2 + 5\gamma_2^4 - 16\alpha^8\right),$$

$$t_{6,1} = -\frac{\gamma_2^6}{32\alpha^{10}}\left(3\gamma_2^2\alpha^{10} - 3\gamma_2^2\alpha^2 + 2\gamma_2^2 - 8\alpha^{10}\right),$$

$$t_{9,1} = \frac{1}{128}\gamma_2^8,$$

$$t_{3,1} = t_{4,1} = t_{7,1} = t_{8,1} = t_{10,1} = 0.$$

Appendix F: Nomenclature

Nomenclature

$\bar{e}_{31}$ The effective longitudinal e-form piezoelectric coupling factor.

α The ratio γ_1/γ_2.

α_H The upper limit of the normalized radius r.

α_L The lower limit of the normalized radius r.

δH The virtual variation of the electrical enthalpy.

δW The virtual variation of the potential energy due to external applied forces.

δw_0 The virtual variation in the displacement w_0.

$\Gamma(\cdot)$ The Gamma function.

γ_0 The ratio of the reference circle diameter to the square plate side a.

γ_1 The ratio of the pupil opening diameter to the square plate side a.

γ_2 The ratio of the fictitious circle diameter to the square plate width a.

Γ_{Ω_i} A boundary separate two subdomains.

λ light wavelength.

$\mathbf{A}_{\mathrm{II}}$ The coefficients vector in domains Ω_{II} and Ω_2. Its size is $2N_L \times 1$.

$\mathbf{A}_{\mathrm{I}}$ The coefficients vector in domains Ω_{I} and Ω_1. Its size is $N_L \times 1$.

$\mathbf{C}$ The Gegenabuer coefficient vector of size $N_G \times 1$.

$\mathbf{D}^*$ Modified flexural rigidities matrix.

$\mathbf{H}^{I_i}$ The ith variational integral written in matrix form.

$\mathbf{H}_n^{I_i}$ The nth submatrix of the $\mathbf{H}^{I_i}$.

$\mathbf{T}_1$ Transformation matrix between coefficients in the domains Ω_1 and Ω_2 in model 1.

$\mathbf{T}_{\mathrm{II}}$ Transformation matrix between coefficients in the domains Ω_{II} and Ω_{III} in model 2.

$\mathbf{T}_{\mathrm{I}}$ Transformation matrix between coefficients in the domains Ω_I and Ω_{II} in model 2.

$\mathrm{d}\hat{\mathbf{n}}$ The differential length vector normal to the lens' outer boundary Γ_Ω.

Ω The lens' planar domain.

Ω_i A subdomain of the planar domain Ω.

$\overline{z}_\mathrm{p}$ The distance between the center of the piezoelectric layer and the reference plane.

Φ_k The single-indexed Gegenbauer polynomial in the cartesian form.

ϕ_{lj} The double-indexed weighted Gegenbauer polynomial in the cartesian form.

$\widetilde{\Phi}_k$ The single-indexed weighted Gegenbauer polynomial in the polar form.

ζ_w l_2 relative error norm for the displacement.

$\zeta_{1/F\#}$ l_2 relative error norm for the reciprocal of F-number.

ζ_{RMSWFE} l_2 relative error norm for the RMSWFE.

a The side length of the square diaphragm.

$A_i^\mathrm{II}, B_i^\mathrm{II}, C_i^\mathrm{II}, D_i^\mathrm{II}$ coefficients of $w_0^{(II)}$.

$A_i^\mathrm{I}, B_i^\mathrm{I}$ coefficients of $w_0^{(1)}$ and $w_0^{(I)}$.

b_{lj} The normalization factor for polynomial ϕ_{lj}.

D_{ij,Ω_i}^* Modified flexural rigidities for the subdomain Ω_i.

D_{ij}^gl Flexural rigidities for the glass layer only.

D_{ij}^p Flexural rigidities for the piezoelectric layer only.

$f'_{k,n}(r, \gamma_0)$ The derivative of the nth Fourier coefficient for the kth Gegenbauer basis function with

respect to the variable r.

$F\#$ F-number.

$f_{k,n}(r, \gamma_0)$ The nth Fourier coefficient for the kth Gegenbauer basis function.

N The number Gegenbauer polynomials in X or Y directions.

n Fourier index ranging from 2 to N_F.

N_L The number of coefficients for the subfunctions $w_0^{(1)}$.

N_F The maximum order of Fourier series terms to fully expand set of N_G weighted Gegenbauer

polynomials.

N_G The number of DOFs for the variational models.

$N_{s,k}$ The sufficient order of Fourier series terms to fully expand the basis function Φ_k.

$N_{s,lj}$ The sufficient order of Fourier series terms to fully expand a doubled-indexed Gegenbauer

polynomial ϕ_{ij}.

r, θ Normalized polar coordinates.

$RMSWFE$ RMS-wavefront-error.

V_{p} The actuation voltage applied across the piezoelectric stack.

w_0 Displacement in the z-direction.

w_{FEM} FEM simulation for the displacement in the z-direction.

w_{N_G} The variational solution for the displacement in the z-direction with N_G basis functions.

x, y Cartesian coordinates.

X, Y Normalized Cartesian coordinates.

C_k The Gegenabuer coefficient for the polynomial Φ_k.

$F_\circ$ The force variational integral over an annular (or circular) subdomain.

F_{Ω_i} The force variational integral over a subdomain Ω_i.

$F_\square$ The force variational integral over a square cartesian subdomain.

$R_\circ$ The spring variational integral over an annular (or circular) subdomain.

R_{Ω_i} The spring variational integral over a subdomain Ω_i.

$R_\square$ The spring variational integral part over a square subdomain.

Mahmoud A. Farghaly is currently a PhD researcher at the University of Southeast Norway. He received his BA and MSc degrees in Electrical Engineering from Assiut University, Egypt in 2010 and 2013, respectively. His current research interests include design and modeling of MEMS sensors and actuators for mobile phones such as: (Lorentz-force and inductive) magnetometers and piezoelectric actuators.

Ulrik Hanke (SM06) received the Siv.Ing. degree and the Dr.Ing. degree in physics from the Norwegian University of Science and Technology (NTNU), Trondheim, Norway, in 1989 and 1994, respectively. After two years as a Post-Doctoral Researcher, he worked for a decade as a Research Scientist with the Department of Communication Technology, SINTEF. Since 2006, he

has been with(University College until 2018) University of Southeast Norway, Horten, where he is currently a Professor of Micro- and Nanosystem Technology. His current main research interest is in the theory, design, and modeling of piezoelectric and RF acoustic micro devices.

Muhammad Nadeem Akram is a professor at the University of Southeast Norway. He obtained Ph.D. degree in photonics from Royal Institute of Technology, Stockholm Sweden in 2005. His research interests are: semiconductor lasers, imaging optics, laser projectors and speckle reduction.

Einar Halvorsen is a professor of micro- and nanotechnology at the University of Southeast Norway. He received the Siv.Ing. degree in physical electronics from the Norwegian Institute of Technology (NTH) in 1991, and the Dr.Ing. degree in physics from the Norwegian University of Science and Technology (NTNU, formerly NTH) in 1996. Since then, he has worked both in academia and the microelectronics industry. His current research interests are in theory, design, and modelling of microelectromechanical devices.

Biographies and photographs of the other authors are not available.

List of Figures

List of Tables